Simulations of Rotating Anelastic Convection: Entropy Boundary Conditions

by

Keith Cuff

A thesis submitted in partial fulfillment of the requirements for the degree of

Master of Science

in

Geophysics

Department of Physics

University of Alberta

Abstract

In this dissertation we focus on numerical models of rotating anelastic convection, in particular the entropy boundary condition, with application to the giant planets. The first chapter details atmospheric features of giant planets and the numerical formulation of anelastic convection. The second chapter details entropy gradient boundary conditions compared to constant entropy boundary conditions used in previous studies. The third chapter considers a Gaussian perturbation on the lower boundary condition to examine surface effects of a plume from the deep interior. The fourth chapter considers high resolution simulations that are closer to a planetary parameter space.

Most previous works on models of anelastic convection use a constant entropy difference boundary condition. For a strongly stratified system this requires a large entropy gradient near the surface to maintain the difference. This makes for strong convection at the outer boundary that disrupts coherent vortices. We use constant entropy gradient boundary conditions with entropy sinks so that the convection is strongest at the inner boundary and grades into neutral buoyancy at the outer boundary.

A thermal plume from the deep interior is modelled using a Gaussian perturbation on the lower boundary. The parametrization of the plume is examined considering its amplitude, width, the latitudinal offset, and the background convective state. The flow produced at the surface typically includes a constant cyclonic vortex at the pole and short lived anticyclones at a lower latitude.

Lowering the Ekman number allows for models that are less viscous and more representative of planets. These models have relaxation oscilations that are relatively quiet at the minimum and produce strong storms at the peak. We use these models to study the quasiperiodic Great White Spot storms that are observed on Saturn with a periodicity of about 1 Saturnian year.

Acknowledgments

To my supervisor Moritz Heimpel for supporting me, providing me with a vast amount of knowledge pertaining to anelastic convection, and for assistance in editing my thesis. To my other committee members Doug Scmitt, Bruce Sutherland, and Morris Flynn for reading my thesis and providing feedback. This work was made possible with the computational resources of the regional organizations Westgrid and Calcul Québec.

Contents

List of Tables

List of Figures

Symbol	Description	Page
Y	Helium mass mixing ratio	2
R_J	Radius of Jupiter	3
R_S	Radius of Saturn	3
r_i	Inner spherical radius	7
r_o	Outer spherical radius	7
$\hat{\mathbf{z}}$	Axis of rotation	7
Ω	Rate of rotation	7
$\hat{\theta}$	Latitudinal unit vector	7
$\hat{\phi}$	Azimuthal unit vector	7
$\hat{\mathbf{r}}$	Radial unit vector	7
ρ	Density	7
$\mathbf{u}$	Velocity	8
p	Pressure	8
ν	Kinematic viscosity	8
α	Thermal expansivity	8
g	Gravity	8
κ	Thermal diffusivity	8
T	Temperature	8
d	Length scale	8
ΔT	Temperature scale	9
Ra	Rayleigh number	9
E	Ekman number	9
Pr	Prandtl number	9
η	Radius ratio	11
m	Polytropic index	11
γ	Ratio of specific heat capacities	11
c_p	Specific heat capacity at constant pressure	
c_v	Specific heat capacity at constant volume	
N_ρ	Density stratification parameter	11
Δs	Entropy scale	11
s	Entropy	12
θ	Potential temperature	12
H	Entropy sink	12
S	Rate of strain tensor	12
Di	Dissipation parameter	12
Ra_c	Critical Rayleigh number	13
Q_s	Heat flux entropy contribution	13
β_i	Inner boundary entropy gradient	13
Ra_f	Flux based Rayleigh number	13

Symbol	Description	Page
Ra^*	Modified Rayleigh number	13
Ra_f^*	Flux based modified Rayleigh number	13
W	Mass flux toroidal potential	14
Z	Mass flux poloidal potential	14
Δ_H	Horizontal Laplacian component	15
∇_H	Horizontal divergence component	15
Y_l^m	Spherical harmonic functions	15
l	Spherical harmonic degree	16
m	Spherical harmonic order	16
P_l^m	Associate Legendre polynomials	16
δ_{ij}	Kronacker delta function	16
l_{max}	Maximum degree of spherical harmonic expansion	16
N_θ	Number of latitudinal grid points	17
N_ϕ	Number of azimuthal grid points	17
w_j	Gaussian quadrature weights	17
$C_n(x)$	Chebyshev polynomial of degree n	17
N	Max degree of Chebyshev expansion	16
N_r	Number of radial grid points	18
$I(x,t)$	Implicit timestepping terms	19
$E(x,t)$	Explicit timestepping terms	19
$d(l)$	Hyperdiffusivity function	20
α	Hyperdiffusivity amplitude	20
β	Hyperdiffusivity exponent	20
$\mathcal{R}$	Depth dependent Rayleigh number	27
s_c	Conductive entropy	27
β	Coriolis parameter	33
λ	Latitude	33
Υ	Dynamic stability	35
A	Nonhomogeneous boundary amplitude	50
B	Nonhomogeneous boundary background	50
θ_0	Nonhomogeneous boundary latitude offset	50
ϕ_0	Nonhomogeneous boundary azimuth offset	50
σ	Nonhomogensous boundary width	50
V	Entropy flux of source	50
Ra_s	Rayleigh number of source	52

Chapter 1

Introduction

This dissertation will focus on numerical models of rotating anelastic convection with application to the Giant planets and in particular Jupiter and Saturn. In section 1.1 we describe the models of the planetary interiors and several features observed on Jupiter or Saturn that may be explained with our model. The Boussinesq approximation was the basis for previous planetary models and it is described in section 1.2 in its dimensional and nondimensional form. The equations for the anelastic model of convection used for this study are detailed in section 1.3. The simulation code used here, MagIC, and the numerical methods used to solve the equations of anelastic convection are detailed in section 1.4.

1.1 Jupiter and Saturn Observations & Interior Models

Of the planets in our solar system the gas giants, Jupiter and Saturn, stand out for their sheer mass. Between the two of them they contain over 90 % of the planetary mass in the solar system (Fortney and Nettelmann, 2010). The first direct observation of Jupiter from spacecraft came from the flyby of Pioneer 10 in 1973. The Galileo spacecraft arrived at Jupiter in 1995 and provided observations until it was deorbited in 2003. Pioneer 11 flew

by Saturn in 1989 and provided measurements of its ionosphere and its atmosphere (Kliore et al., 1980).

The first direct measurement of the magnetic field and magnetosphere of Jupiter came from the Pioneer 10 flyby. The field was observed to be dipolar with a tilt of between 8°and 15°. The magnetosphere is modelled as a annular current sheet to first order, however it is warped near the equator (Smith et al., 1974). This produces a time dependent behaviour that can be used to infer the rotation of the deep interior. The three pre-Cassini flybys measured the magnetic field of Saturn to be dipolar and closely aligned with the axis of rotation. The Saturn Kilometric radiation was measured to have a period of 10 hours, 39 minutes by Voyager and has been associated with the deep interior (Desch and Kaiser, 1981). However observations from Cassini show that the period varies by 1% and is now 8 minutes longer than the Voyager measurements. This variation is larger than any real variation in the rotation of the interior (Del Genio et al., 2009).

Models of the interior structure and composition of Jupiter and Saturn are uncertain and dependent on a number of constraints. The gravitational and magnetic field morphologies, expressed as spherical harmonic coefficients, the rate of rotation, luminosity, polar radius, and equatorial radius are observational constraints. The abundance of hydrogen, helium, and other heavy elements in the interior and their equation of state are constraints that are not directly observable. The presence of a magnetic field implies that there is dynamo action in the deep interior driven by a conductive fluid. The three-layer model is commonly applied to the giant planets and divides them into: (i) a poorly conductive molecular envelope that includes the atmosphere, (ii) a deeper metallic hydrogen layer that drives the dynamo, and (iii) an inner core of unknown higher density elements (Guillot et al., 2004). For Jupiter the molecular envelope extends to a depth of about 2 Mbar and the helium mass mixing ratio is $Y \simeq 0.23$. The deep atmosphere with metallic

hydrogen has a helium mass mixing ratio of $Y \simeq 0.27$ to match the protosolar H/He ratio (Guillot and Gautier, 2015). Jupiter may or may not have a core. For Saturn the molecular envelope has a helium mass mixing ratio estimation of $Y \simeq 0.20$ and a depth of 2 Mbar. This is deeper compared to Jupiter because Saturn is less massive. The metallic hydrogen layer has a helium mass mixing ratio estimation of $Y \simeq 0.30$ (Guillot and Gautier, 2015). Saturn has a core of uncertain mass.

Empirical models of the interior can be constructed using the observational constraints. Helled et al. (2009) constructed an empirical model of Saturn's density matching the gravitational harmonic coefficients and the atmospheric boundary conditions. The empirical model is compared to an equation of state (EOS) of a hydrogen and helium mixture to interpret the abundance of helium and heavier elements in the interior. The boundary between layers (i) and (ii) is determined by the EOS and electrical conductivity of hydrogen at depth. As the conductivity increases the Ohmic dissipation becomes significant and slows the fluid relative to the molecular envelope. The transition of hydrogen from a molecular to a metallic state has been observed in shock experiments (Nellis et al., 1995) to be continuous, which implies that there is not a sharp transition at the boundary. The material properties of hydrogen and helium at high temperature and pressure can also be explored numerically with ab-initio simulations. French et al. (2012) model the EOS of Jupiter as a linear combination of hydrogen, helium, and water to represent heavier elements. This model predicts a rapid radial decrease in electrical conductivity, starting at a radius of $0.9R_J$ that sets a lower limit of $0.8R_J$ for the full ionization of hydrogen. The depth of the transition for deep models of zonal flow can also be constrained by limiting the depth of Ohmic dissipation such that it does not exceed the luminosity of the planet. This approach sets the depth at $0.96R_J$ and $0.86R_S$ respectively for Jupiter and Saturn (Liu et al., 2008).

There is some debate over the mechanisms that drive jets and storms in the atmosphere of Jupiter and Saturn. Large scale zonal flow is produced by the cascade from small scale turbulence to larger scales in rotating spherical flow (Rhines, 1975). There are two models for atmospheric flow differing on how deep into the interior the jets exist. Shallow models suggests that the flow is quasi-barotropic such that it does not depend on the vertical structure and is confined to a two dimensional weather layer (Williams, 1978). These models have been successful in reproducing latitudinal jets, however they typically produce a retrograde equatorial jet rather then the observed prograde equatorial jet for Jupiter and Saturn. More recent models have been able to achieve a prograde equatorial jet with additional forcing and dissipation (Scott and Polvani, 2008).

In deep models the jets are forced by thermal convection in the interior and are the surface manifestation of Taylor columns that extend axially across both hemispheres outside of the tangent cylinder determined by the transition of molecular to metallic hydrogen (Busse, 1976). Heimpel et al (2005) extend Busse's model to include the transition from the molecular layer into the metallic interior, truncating the Busse columns inside of the tangent cylinder.

The tangent cylinder is the imaginary cylinder that is tangent to the inner boundary at the equatorial plane and has an axis of symmetry parallel to the axis of rotation. This divides the flow into three distinct regions: the northern region inside the tangent cylinder, the equatorial region outside the cylinder, and the southern region inside of the tangent cylinder. The radius ratio η sets the location of the tangent cylinder and is representative of the depth of the molecular envelope. In the equatorial region outside the tangent cylinder a strong prograde jet develops. Inside the tangent cylinder at higher latitudes multiple alternating jets are developed.

More recent studies use the anelastic approximation to incorporate density stratification

(Gastine and Wicht, 2012) and have been able to model storms (Heimpel et al., 2016). The descent of the Galileo probe into the atmosphere of Jupiter measured the zonal wind speed to be increasing to a depth of 4 bars and relatively constant afterwards until the link to the probe was lost at 21 bars, approximately 150km below the cloud tops (Atkinson et al., 1998). The axisymmetric zonal gravitational coefficients may be able to determine the depth of the flow. The jets are not latitudinally symmetric across the equator and therefore the odd degree gravitational zonal harmonics should be nonzero if the flow is deep. However measuring these harmonic coefficients requires a polar orbit. Future gravity measurements from Juno and the final Cassini mission may be precise enough to estimate the wind depth (Galanti and Kaspi, 2015).

The Cassini spacecraft has been orbiting Saturn since mid 2004 and providing observations of its atmosphere, rings, satellites, and magnetosphere. Atmospheric observations include the zonal flow of the planet's jets, the hexagon at the North pole, and the large convective storm of 2010 (Rojas et al., 2000; Baines et al., 2009; Sayanagi et al., 2013).

The hexagon structure at the North pole of Saturn was an unexpected discovery by the Voyager probes (Godfrey, 1988). The flow of clouds in this latitude is of the order 100 m/s however the hexagon appears stationary in the frame of the radio rotation period (Godfrey, 1988). Images taken from Cassini show that this feature remains 28 years later after nearly a Saturnian year (Baines et al., 2009). There are several possible mechanisms for the formation of the hexagon. Allison *et. al.* (1990) suggest that it is a stationary Rossby wave jet that is perturbed by an anticyclonic vortex to the south. Another theory is that the hexagon results from barotropic instability of the high latitude retrograde jets. Analysis of the stability of an idealized zonal jet shows that the prograde eastward jets are more stable than the retrograde westward jets (Howard and Drazin, 1964). Laboratory models of barotropic instability have been able to reproduce a hexagon and other polygonal

shapes using differential rotation (Aguiar et al., 2010) or by pumping fluid at the lower boundary (Sommeria et al., 1991). In the mid-northern latitude of Saturn there is a "ribbon" wave that has been observed by the Voyager probes that was still visible 14 years later (Sanchez-Lavega, 2002). It is suggested that this feature is also a result of barotropic instability (Godfrey and Moore, 1986).

Saturn experiences quasi-periodic giant storms known as the Great White Spots (GWS). Observations of Saturn have recorded instance of the GWS occurring in 1903, 1933, and 1960 (Sánchez-Lavega and Battaner, 1986). The storms alternate between mid-latitude and equatorial regions and are observed with a period of roughly 30 years, which corresponds to one year of Saturn. In 1990 the GWS erupted near the equator and was observed in detail by the Hubble Space Telescope(Sánchez-Lavega et al., 1991). It was initially observed as a bright spot located in the interface between the equatorial zone and the north equatorial belt. There was counterdirectional zonal expansion at the northeast and southern extremities produced by zonal wind shear. The initial spot continued to grow and developed a distinct double nucleus. Over time the two cloud fronts expanded in opposite direction and covered most of the northern equatorial belt eventually merging. Nearly a month later dark spots were observed in regular intervals at 18°N, bright spots were observed to the south at 10.5°N, and more dark spots were observed at 5.5°N.

In December 2010 a planet-encircling convective storm was observed at mid latitude from the orbit of Saturn by the spacecraft Cassini (Sayanagi et al., 2013). Prior to the start of the storm a feature known as the String of Pearls was observed at latitudes between 32.5°N and 34.5°N. The pearls can be seen as a band of dark spots in the visible band and bright spots in the infrared spectrum. They are interpreted to be holes in the cloud layer from which thermal radiation from the interior is released. After the storm erupted it was characterized by three distinct parts. The westernmost bright cloud is the head of the

storm and is trailed to the east by a large anticyclonic vortex (AV). Further to the east of the AV is the tail of the storm where the clouds are turbulent without well defined edges. The head of the storm drifted to the west of the AV and eventually collided with it after circling the planet.

1.2 Equations of Boussinesq Convection

Thermal convection describes the flow of fluid that is heated at the bottom and cooled at the top. This can be a good approximation for the flow of fluid in planets and stars. The fluid motion is described by a self consistent set of equations given by conservation laws. The conservation of momentum, energy, and mass form a complete set of equations with a unique solution when the boundary conditions are specified. The velocity boundary conditions are impenetrable across the boundary and the tangent flow boundary condition may be no-slip or free-slip. The thermal boundary condition may be constant temperature or constant temperature gradient across the boundaries.

The Boussinesq approximation assumes that the density variations in a fluid are negligible except in the buoyancy term. This approximation is commonly used for modelling convection in Earth's liquid core and for dynamo models of terrestrial planets (Christensen and Wicht, 2007) and for models of deep convection in planets (Christensen, 2001; Heimpel and Aurnou, 2012; Heimpel and Gómez Pérez, 2011). The equations of convection describe the flow of a fluid in a spherical shell of inner radius r_i and outer radius r_o that is rotating in the $\hat{\mathbf{z}}$ direction with rotation rate Ω. The spherical geometry of the model is shown in figure 1.1. The spherical coordinate convention used here is azimuthal direction $\hat{\phi}$, co-latitude $\hat{\theta}$, and radial direction $\hat{\mathbf{r}}$. The tangent cylinder is the imaginary surface that is tangent to the inner boundary at the equatorial plane and has an axis of symmetry parallel to the axis of rotation. The conservation of mass for a fluid with density ρ and a velocity

$\mathbf{u}$ is given by the continuity equation:

$$\frac{\partial \rho}{\partial t} + \nabla \cdot \rho \mathbf{u} = 0 \tag{1.1}$$

Under the Boussinesq approximation ρ is a constant background density, thus this reduces to the flow being divergence free,

$$\nabla \cdot \mathbf{u} = 0. \tag{1.2}$$

The conservation of momentum is given by the Navier-Stokes equation in a rotating reference frame with radial gravity:

$$\frac{\partial \mathbf{u}}{\partial t} + \mathbf{u} \cdot \nabla \mathbf{u} = -\frac{1}{\rho}\nabla p - 2\boldsymbol{\Omega} \times u + \alpha g T + \nu \nabla^2 \mathbf{u}, \tag{1.3}$$

Where p is the pressure, ν is the kinematic viscosity, α is the coefficient of thermal expansivity, and g is gravity. The conservation of energy is given by:

$$\frac{\partial T}{\partial t} + \mathbf{u} \cdot \nabla T = \kappa \nabla^2 T, \tag{1.4}$$

Were κ is the thermal diffusivity and T is the variable temperature.

1.2.1 Non-dimensionalized Equations

The system of equations (1.2 - 1.4) can be nondimensionalized by characteristic scales to help understand the relative importance of the differing terms.

The characteristic length scale d is taken to be the radial distance across the spherical shell $r_o - r_i$, the time scale is taken to be the thermal diffusion time d^2/κ, the reference velocity is therefore κ/d, and the reference temperature is scaled according to the difference

across the shell ΔT. The relations between dimensional and nondimensional (starred) parameters are given by:

$$x = x^* d \qquad t = t^* \frac{d^2}{\kappa} \qquad u = u^* \frac{\kappa}{d} \qquad T = T^* \Delta T \qquad p = p^* \frac{\rho \nu \kappa}{d^2} \tag{1.5}$$

Where starred parameters are nondimensional. Substituting the nondimensional variables into the momentum equation gives

$$\frac{\kappa^2}{d^3}\left(\frac{\partial \mathbf{u}^*}{\partial t^*} + \mathbf{u}^* \cdot \nabla \mathbf{u}^*\right) = \frac{1}{\rho}\frac{\rho \nu \kappa}{d^2}\nabla p^* - \frac{2\Omega\kappa}{d}(\hat{\mathbf{z}} \times \mathbf{u}^*) + \alpha g \Delta T T^* + \frac{\nu\kappa}{d^3}\nabla^2 \mathbf{u}^*. \tag{1.6}$$

We then divide through by $\kappa\nu/d^3$ to get

$$\frac{\kappa}{\nu}\left(\frac{\partial \mathbf{u}^*}{\partial t^*} + \mathbf{u}^* \cdot \nabla \mathbf{u}^*\right) = \nabla p^* - 2\frac{d^2\Omega}{\nu}(\hat{\mathbf{z}} \times \mathbf{u}^*) + \frac{\alpha g \Delta T d^3}{\kappa\nu} T^* + \nabla^2 \mathbf{u}^* \tag{1.7}$$

from here we can define three nondimensional parameters: the Rayleigh Number Ra which is the ratio of buoyancy to diffusivity, the Ekman Number E which is the ratio of viscous diffusion to rotation, and the Prandtl Number Pr which is the ratio of viscous to thermal diffusivity.

$$Ra = \frac{\alpha g \Delta T d^3}{\nu \kappa} \tag{1.8}$$

$$E = \frac{\nu}{\Omega d^2} \tag{1.9}$$

$$Pr = \frac{\nu}{\kappa} \tag{1.10}$$

this gives the nondimensional form of the momentum equation as

$$\frac{1}{Pr}\left(\frac{\partial \mathbf{u}^*}{\partial t^*} + \mathbf{u}^* \cdot \nabla^* \mathbf{u}^*\right) = \nabla p^* - \frac{2}{E}(\hat{\mathbf{z}} \times \mathbf{u}^*) + RaT^* + \nabla^2 \mathbf{u}^*. \tag{1.11}$$

Substituting the nondimensional variables into the temperature equation gives

$$\frac{\kappa \Delta T}{d^2}\left(\frac{\partial T^*}{\partial t^*} + \mathbf{u}^* \cdot \nabla T^*\right) = \frac{\kappa \Delta T}{d^2}\nabla^2 T^*, \tag{1.12}$$

divide through by $\kappa \Delta T/d^2$ to get

$$\frac{\partial T^*}{\partial t^*} + \mathbf{u}^* \cdot \nabla T^* = \nabla^2 T^*. \tag{1.13}$$

The conservation of mass equation remains unchanged,

$$\nabla \cdot \mathbf{u}^* = 0. \tag{1.14}$$

For subsequent nondimensional equations we drop the star notation.

1.3 Equations of Anelastic Convection

The Boussinesq approximation assumes that density variations are negligible except in the buoyancy term while a fully compressible model would require a small enough timestep to resolve sound waves. Between these two models is the anelastic approximation which allows for a background density contrast while filtering out sound waves. In this formulation the time dependence of the thermodynamic variables is eliminated, except for entropy (Lantz and Fan, 1999). This simplifies the equations and reduces the computational workload. The anelastic approximation holds provided the velocity of the flow is not comparable to the speed of sound.

We derive our anelastic formulation following Jones et al. (2011) and Gastine & Wicht (2012). The anelastic approximation expands thermodynamic properties temperature T, density ρ, and pressure p as the sum of a adiabatic background (bar) and a perturbation (primed).

$$T = \bar{T} + T', \ \rho = \bar{\rho} + \rho', \ p = \bar{p} + p'. \tag{1.15}$$

Mass is assumed to be concentrated inside the interior such that $g \propto \frac{1}{r^2}$ in the molecular shell. The background state for the temperature and pressure is given by

$$\bar{T}(r) = \frac{c_0}{(1+\eta)r} + 1 - c_0 \quad \text{and} \quad \bar{\rho} = \bar{T}^m, \tag{1.16}$$

with

$$c_0 = \frac{\eta}{1-\eta}\left(\exp\frac{N_\rho}{m} - 1\right). \tag{1.17}$$

With radius ratio is $\eta = r_i/r_0$ and polytropic index m. Following Gastine and Wicht (2012) we use $m = 2$. This choice of polytropic index generates a density-temperature relation that approximates giant planet interior models. In a dimensional formulation the polytropic index m is related to the ratio of specific heat capacities $\gamma = c_p/c_v$ by $\gamma = (n+1)/n$. The density stratification is given by

$$N_\rho = ln(\bar{\rho}(r_i)/\bar{\rho}(r_o)), \tag{1.18}$$

where N_ρ is the number of density scale heights between r_i and r_o.

The equations are formulated in nondimensional form with a length scale set by the shell thickness $d = r_o - r_i$, a time scale set by the viscous diffusion time d^2/ν, and an entropy scale set by the difference Δs across the boundaries. Temperature, density, and

gravity are scaled according to their value at the outer boundary. The energy equation is formulated so that the entropy s is the thermodynamic variable rather than the temperature T used in the Boussinesq approximation. In atmospheric convention it is common to use potential temperature θ as an thermodynamic variable which is related to entropy through $s = c_p \ln \theta$.

The equations for conservation of momentum, energy, and mass for the anelastic approximation are given by:

$$E\left(\frac{\partial \mathbf{u}}{\partial t} + \mathbf{u}\cdot\nabla\mathbf{u}\right) + 2\hat{\mathbf{z}}\times\mathbf{u} = -\nabla\frac{p'}{\bar{\rho}} + \frac{RaE}{Pr}\frac{r_o^2}{r^2}s\hat{\mathbf{r}} + \frac{E}{\bar{\rho}}\nabla\cdot S, \tag{1.19}$$

$$\bar{\rho}\bar{T}\left(\frac{\partial s}{\partial t} + \mathbf{u}\cdot\nabla s\right) = \frac{1}{Pr}(\nabla\cdot(\bar{\rho}\bar{T}\nabla s) + H\bar{\rho}\bar{T}) + Di\bar{\rho}S^2, \tag{1.20}$$

$$\nabla\cdot(\bar{\rho}\mathbf{u}) = 0. \tag{1.21}$$

Where H is a constant entropy source or sink, and S is the traceless rate-of-strain tensor given by

$$S_{ij} = 2\bar{\rho}\left(\frac{\partial u_i}{\partial x_j} + \frac{\partial u_j}{\partial x_i} + \frac{2}{3}\delta_{ij}\nabla\cdot\mathbf{u}\right) \tag{1.22}$$

and Di is the dissipation parameter given by

$$Di = \frac{\eta Pr(e^{N_\rho/m} - 1)}{Ra}. \tag{1.23}$$

In addition to N_ρ and η, the system is governed by three nondimensional parameters: the Rayleigh number Ra, the Ekman number E, and the Prandtl number Pr. In the anelastic formulation the Rayleigh number is :

$$Ra = \frac{g_0 d^3 \Delta s}{c_p \nu \kappa} \tag{1.24}$$

where c_p is the specific heat capacity and g_0 is the gravity at the inner boundary. The Rayleigh number relates the ratio of buoyancy to dissipation and is a measure of how convective the system is. If $Ra < Ra_c$, the critical Rayleigh number heat transport is primarily through conduction, if $Ra > Ra_c$ heat transport is primarily through convection. For our models we use constant entropy gradient boundary conditions. Note that in dimensional form the entropy gradient contributions to the heat flux is given by $Q_s = -\kappa \bar{\rho} \bar{T} \nabla (\bar{s} + s)$.

We define a flux based Rayleigh Number that is scaled based on the inner boundary entropy gradient rather than the difference in entropy across the shell:

$$Ra_f = \frac{g_0 d^4 |\beta_i|}{c_p \nu \kappa}, \tag{1.25}$$

where β_i is the entropy gradient at the inner boundary. In systems with strong rotation and low viscosity it is useful to consider a modified Rayleigh number Ra^* that relates buoyancy to rotation:

$$Ra^* = \frac{g_0 \Delta s}{c_p \Omega d}. \tag{1.26}$$

This definition is slightly different from the Boussinesq case because the energy equation is formulated in terms of the entropy instead of the temperature. The flux based counterpart for the modified Rayleigh number is given by:

$$Ra_f^* = \frac{g_0 |\beta_i|}{c_p \Omega}. \tag{1.27}$$

The Ekman number E and the Prandtl number Pr have the same definition as in the

Boussinesq case. The modified Rayleigh number can be related to the standard Rayleigh number with the relation

$$Ra^* = RaE^2Pr^{-1}. \tag{1.28}$$

This expression also holds for the flux based Rayleigh number.

1.4 Numerical Simulations

The numerical simulations are solved using the anelastic and nonmagnetic mode of the magnetohydrodynamic code MagIC. MagIC is free software licensed under the GPLv3 and is available at https://github.com/magic-sph/magic. The code originates in Glatzmaier's stellar dynamo code (Glatzmaier, 1984). Johannes Wicht modified it to include the presence of an inner core (Wicht, 2002) and Gastine implemented the anelastic approximation (Gastine and Wicht, 2012). The latest version of the code implements the SHTns library for spherical harmonic transforms (Schaeffer, 2013). MagIC has been benchmarked against other dynamo codes (Jones et al., 2011; Christensen et al., 2001; Breuer et al., 2010). The following descriptions of the numerical method employed are based on the MagIC documentation.

1.4.1 Poloidal and Toroidal Decomposition

Magic is a pseudospectral code that operates in both spectral space and in grid space. A vector field that has no divergence is called a solenoidal field and can be decomposed into a toroidal and a poloidal potential. In the anelastic approximation the mass flux is decomposed into a poloidal potential W and a toroidal potential Z giving:

$$\bar{\rho}\mathbf{u} = \nabla \times (\nabla \times W\mathbf{e_r}) + \nabla \times Z\mathbf{e_r}. \tag{1.29}$$

This decomposition has the advantage of automatically satisfying the continuity equation reducing the system from three to two equations.

The horizontal component of the spherical Laplacian Δ_H is given by

$$\Delta_H = \frac{1}{r^2 sin\theta}\frac{\partial}{\partial\theta}\left(sin\theta\frac{\partial}{\partial\theta}\right) + \frac{1}{r^2 sin^2\theta}\frac{\partial^2}{\partial^2\phi}, \tag{1.30}$$

and the horizontal component of the divergence operator ∇_H is given by

$$\nabla_H = rsin\frac{\partial(sin\theta)}{\partial\theta}\mathbf{e}_\theta + rsin\frac{\partial}{\partial\phi}\mathbf{e}_\phi. \tag{1.31}$$

Using these the expression for the mass flux $\bar{\rho}\mathbf{u}$ in terms of the poloidal and toroidal potential becomes

$$\bar{\rho}\mathbf{u} = -\Delta_H\mathbf{e_r}W + \nabla_H\frac{\partial}{\partial r}W + \nabla_H \times \mathbf{e_r}Z. \tag{1.32}$$

The expression for the curl of the mass flux is also useful and is given by:

$$\nabla \times \bar{\rho}\mathbf{u} = -\Delta_H\mathbf{e_r}Z + \nabla_H\frac{\partial}{\partial r}Z + \nabla_H \times \Delta_H\mathbf{e_r}W. \tag{1.33}$$

1.4.2 Spherical Harmonic Representation

The spherical harmonic functions Y_l^m form an orthogonal basis on the surface of a sphere and are the natural choice for the horizontal expansion in colatitude θ and longitude ϕ and are given by:

$$Y_l^m(\theta,\phi) = P_l^m(\cos\theta)e^{im\phi}. \tag{1.34}$$

Where l and m are the spherical harmonic degree and order respectively and P_l^m is the associated Legendre function. There are several conventions for normalization of the spherical harmonic functions. MagIC adopts a complete normalization with the orthogonality given by

$$\int_0^{2\pi}\int_0^{\pi} Y_l^m(\theta,\phi)Y_{l'}^{m'}(\theta,\phi) = \delta_{ll'}\delta^{mm'}, \tag{1.35}$$

where δ_{ij} is the Kronecker delta.

The fully normalized spherical harmonic functions are given by

$$Y_l^m(\theta,\phi) = \sqrt{\frac{1}{2\pi}}\frac{(2l+1)(l-|m|)!}{2(l+|m|)!}P_l^m(\cos\theta)e^{im\phi}(-1)^m. \tag{1.36}$$

For example, the spherical harmonic representation of the poloidal potential $W(r,\theta,\phi)$ truncated at degree l_{max} is given by

$$W(r,\theta,\phi) = \sum_{l=0}^{l_{max}}\sum_{m=-l}^{l} W_{lm}(r)Y_l^m(\theta,\phi). \tag{1.37}$$

The transformation from grid space into spherical harmonic space is given in two steps

$$W_{lm}(r) = \frac{1}{\pi}\int_0^{\pi} W_m(\theta,\phi)P_l^m(\cos\theta)\sin\theta d\theta, \tag{1.38}$$

$$W_m(r,\theta) = \frac{1}{2\pi}\int_0^{2\pi} W(r,\theta,\phi)e^{-im\phi}. \tag{1.39}$$

The potential function $W(r,\theta,\phi)$ is a real function such that the spherical harmonic

coefficients are symmetric under conjugation $W_{lm^*} = W_{l,-m}$, where $*$ denotes complex conjugation. Therefore only coefficients with $m \geq 0$ need to be considered. In general, all of the potential fields calculated are real so that this symmetry applies to them all. The inverse spherical harmonic transformation from spectral space to grid space $(r, l, m) \rightarrow (r, \theta, \phi)$ is given by equation (1.38). The forward transformation from grid space to spectral space $(r, \theta, \phi) \rightarrow (r, l, m)$ is defined in two steps by equation (1.39) and (1.40). In the longitudinal direction a fast-Fourier transform is employed, requiring a minimum of $N_\phi = 2l_{max} + 1$ evenly spaced grid points in ϕ. In the latitudinal direction the integral (1.39) is solved using Gauss-Legendre quadrature

$$W_{lm}(r) = \frac{1}{N_\theta} \sum_{j=1}^{N_\theta} w_j W_m(r, \theta_j) P_l^m(\cos\theta_j), \tag{1.40}$$

where θ_j are the N_θ Gaussian quadrature points with weight w_j that define the latitudinal grid. Aliasing errors can be avoided by taking the maximum degree of expansion $l_{max}+1 = N_\phi/3$. The spherical harmonic functions have several recurrence relations that are used to compute the Coriolis force and derivatives of advection.

1.4.3 Radial Representation

The radially dependent components of the flow are expanded in terms of Chebyshev polynomials $C(x)$. The polynomials of degree n are defined by

$$C_n(x) = \cos[n \arccos(x)], \qquad -1 \leq x \leq 1. \tag{1.41}$$

The radial expansion of the poloidal component of the mass flux W, truncated to degree N is:

$$W_{lm}(r) = \sum_{n=0}^{N} W_{lmn} C_n(r). \tag{1.42}$$

The forward transform from grid space to spectral space is given by

$$W_{lmn} = \frac{2 - \delta_{n0}}{\pi} \int_{-1}^{1} \frac{W_{lm}(r(x)) C_n(x) dx}{\sqrt{1 - x^2}}. \tag{1.43}$$

The Chebyshev space ($-1 \leq x \leq 1$) is linearly mapped onto the radius range ($r_i \leq r \leq r_o$) using

$$x(r) = 2\frac{r - r_i}{r_o - r_i} - 1. \tag{1.44}$$

The radial grid points can also be mapped nonlinearly to provide a greater density towards the boundaries. The N_r extrema of $C_{N_r - 1}$ are take as the radial grid points,

$$x_k = \cos\left(\pi \frac{(k-1)}{N_r - 1}\right), \qquad k = 1, 2, \ldots, N_r. \tag{1.45}$$

this values of the Chebyshev polynomials at these points are given by:

$$C_{nk} = C_n(x_k) = cos\left(\pi \frac{n(k-1)}{N_r - 1}\right). \tag{1.46}$$

This choice has the advantage of more dense grid points near the boundaries to better resolve thermal and viscous boundary layers and it enables a Fast Fourier Transform between grid space and Chebyshev spectral space. Choosing the number of radial grid points $N_r > N$ avoids aliasing in the radial direction.

1.4.4 Timestepping

The time integration scheme employed is a mixed implicit/explicit algorithm. Implicit timestepping methods offer more stability and allow for larger timesteps however treating the nonlinear terms implicitly couples all spherical harmonic modes and results in a very large matrix inversion. The Coriolis force similarly couples the poloidal and toroidal potentials and some of the spherical harmonic modes. The nonlinear terms and the Coriolis force are treated explicitly and the other terms are treated implicitly. The general differentiation in time can be written as

$$\frac{\partial}{\partial t} + I(x,t) = E(x,t), \tag{1.47}$$

where the implicit terms are denoted by I and the explicit terms are denoted by E. The implicit time step discretization is given by

$$\left(\frac{x(t+\delta t) - x(t)}{\delta t}\right)_I = -\alpha I(x, t+\delta t) - (1-\alpha) I(x,t), \tag{1.48}$$

where α is the weight of the new timestep. The explicit time step uses a second order Adams-Bashforth scheme

$$\left(\frac{x(t+\delta t) - x(t)}{\delta t}\right)_E = \frac{3}{2}E(x,t) - \frac{1}{2}E(x, t-\delta t). \tag{1.49}$$

For the first time step this reduces to a Euler order method which is not as accurate. Combining both steps gives

$$\frac{x(t+\delta t)}{\delta t} + \alpha I(x, t+\delta t) = \frac{x(t)}{\delta t} - (1-\alpha) I(x,t) + \frac{3}{2}E(x,t) - \frac{1}{2}E(x, t-\delta t). \tag{1.50}$$

1.4.5 Other Numerical Considerations

For high resolution runs spherical symmetry in the spherical harmonic coefficients may be employed to improve runtime (for example 2-fold or 4-fold). This is done by calculating only the spherical harmonic order m that are multiples of the symmetry factor. This is equivalent of solving the equations on a fraction of the sphere (for example a hemisphere or quartersphere.) This may effect the flow at high latitudes and cause it to be more axisymmetric. If the flow is dominated by smaller scale longitudinal structure as typical for anelastic convection this assumption should not have a large effect on the solution (Gastine et al., 2013). Spherical symmetry is not used in models that are examining effects at the pole where it would disrupt large scale features (e.g. a polar vortex or polygonal zonal flow).

For strongly convecting low Ekman number simulations sometimes hyperdiffusion is required to ensure convergence of the solution. The diffusive terms in equations (1.5) and (1.6) are operated by an operator of the form

$$d(l) = \left(1 + \alpha \left[\frac{l-1}{l_{max}-1}\right]^{\beta}\right) \tag{1.51}$$

where $d(l)$ is the hyperdiffusivity of spherical harmonic degree l. The amplitude of the hyperdiffusivity is given by α, the hyperdiffusivity exponent is β, and l_{max} is the maximum degree of spherical harmonic expansion. Hyperdiffusivity acts only on the horizontal components and may cause anisotropy with the radial components, and artificial viscous heating. If the amplitude of the hyperdiffusion is small it mainly acts as a low pass filter on the small scale structures. This can be checked by progressively decreasing the amplitude of the hyperdiffusivity after a solution has reached a steady state (Heimpel and Aurnou, 2012).

The convective system is initialized from a conductive state by a random entropy perturbation. For systems that are strongly convecting it is more numerically stable to initialize the system from a previous run that has reached a steady state at a lower Rayleigh number.

1.4.6 Diagnostics & Output

The overall strength of the convection can be determined by examining the kinetic energy timeseries. If the system is subcritical and not convecting the initial energy of the perturbation will decay exponentially. The kinetic energy is divided into the poloidal and the toroidal components of the flow. This is useful because the poloidal component of the flow measures the strength of convection and the toroidal component of the flow will show the development of zonal jets. The background state for the entropy, gravity, and density are useful for understanding the flow near the onset of convection. The full 3d field for the entropy and velocity of the flow can printed however this is often constrained by storage space. For examining the flow temporally it is more practical to save only constant surfaces of interest over time. For large scale features that are independent of the azimuthal direction it is often useful to examine the azimuthal average to smooth out smaller scale features. The velocities in MagIC are typically scaled by the Reynolds number Re which is the ratio of inertial forces to viscous forces. It is often convenient to scale the velocities according to the Rossby number Ro which is the ratio of inertial forces to Coriolis forces. The conversion between the Reynolds number velocity Re and the Rossby number velocity Ro is given by $Ro = ReEk(1 - \eta)$.

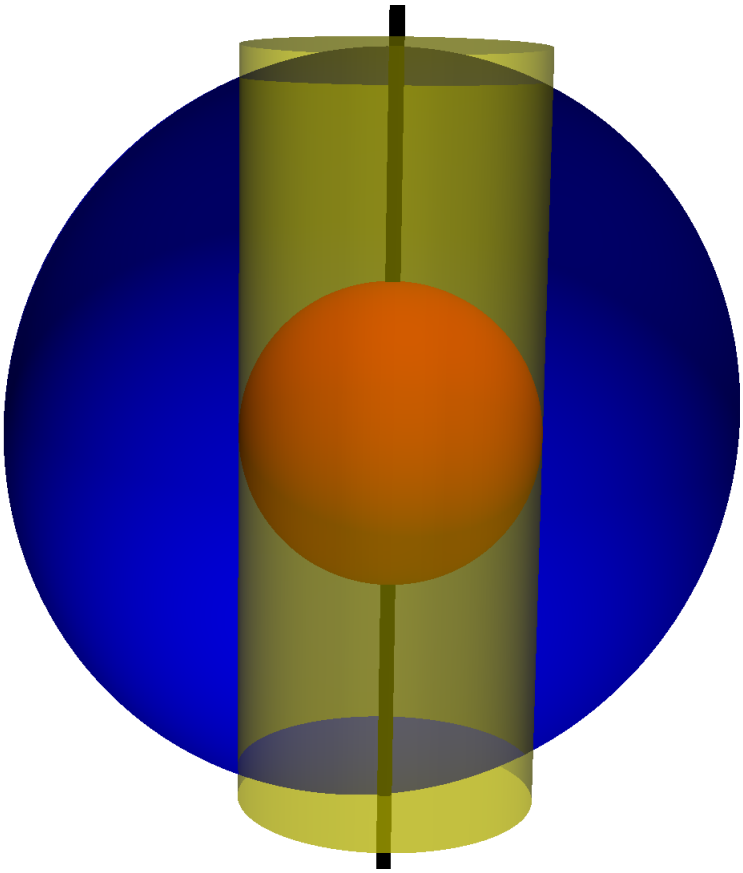

Figure 1.1: Spherical geometry for anelastic simulations. The inner boundary r_i is shown as a red sphere and the outer boundary r_o is shown as blue sphere. The tangent cylinder is shown in yellow and the axis of rotation is marked with a black line. The radius ratio here is for illustrative purposes and not typical for simulations of the molecular envelopes of giant planets.

Chapter 2

Neutral buoyancy surface boundary condition

Compared to the Boussinesq approximation, the anelastic approximation allows for modeling of the density stratification in the giant planets. However the constant entropy boundary conditions with no internal entropy source or sink require a large entropy gradient towards the outer boundary to maintain a constant difference and to balance total heat flux into and out of the sphere. Entropy gradient boundary conditions can be used to reduce or remove the buoyancy from the outer boundary. Here the outer boundary is heated and we use an entropy sink prevent the model from heating over time. This allows for neutral buoyancy or stable stratification near the outer boundary that grades into a convective interior (Heimpel et al., 2016). The buoyant stability of Jupiter was observed by the Galileo probe as it descended into the atmosphere to a depth of 22 bar (Magalhães et al., 2002). The density stratification of Saturn has not been measured directly by a descending probe. However the stability can be constrained by models of vortices (Del Genio et al., 2009).

Near the onset of convection the Rayleigh number is slightly greater than critical. Under the Boussinesq approximation the fluid flows in linear convection cells attached to the inner boundary. To maintain a constant temperature difference across a spherical shell a larger heat flux is required near the inner boundary. This is because the inner boundary has less surface area than the outer boundary in a spherical shell system.

Under the anelastic approximation the entropy gradient required to maintain a constant difference in entropy is inversely proportional to the density of the fluid. For a fluid with a relatively weak density stratification the effects of the spherical geometry dominate and the onset of convection is maintained on the inner boundary. For a fluid with a strong density contrast the effect of the density stratification is significant and the onset of convection begins at the outer boundary.

The strength of convection and the buoyant stability of the flow are controlled by the entropy gradient. When the entropy gradient is positive the system is convective and the strength of convection is proportional to it. When the entropy gradient is negative there is an inversion of the entropy difference and the system is buoyantly stable. A fluid that is stable can produce internal gravity waves. Buoyant stability helps to maintain storms or vortices that would otherwise be dispersed by convection. In numerical models the stability can be controlled by introducing entropy sources and sinks.

In this chapter we present a study of anelastic convection simulations with zero entropy gradient (neutral buoyancy) at the outer boundaries over a range of density stratifications. This allows us to examine the development of zonal flow with neutral buoyancy compared to a previous study with constant entropy boundaries (Gastine and Wicht, 2012). The near onset of convection is examined to show the large difference in the background conductive state. The convective regimes of the system are detailed and compared to previous anelastic and Boussinesq models. The development of zonal jets with increasing density

stratification, and the dynamic buoyant stability of the system over time are also studied.

2.1 Simulation Parameters

The simulations of anelastic convection are dependent on several nondimensional parameters, variables related to the equation of state, and the boundary conditions. The nondimensional parameters are the modified Rayleigh number Ra^*, which measures the strength of thermal convection relative to rotation, the Prandtl number Pr, which measures the ratio of thermal to viscous diffusion, and the Ekman E, which measures the ratio of viscous forces to rotational forces. The equation of state is determined by the polytropic index m which determines the relation between density and temperature, the radius ratio $\eta = r_i/r_o$ which measures the relative geometry of the spherical shell, and the density stratification N_ρ which determines the density contrast across the shell. The thermal boundary conditions allow for constant entropy or constant entropy gradient conditions and the mechanical boundary conditions can be no-slip or free-slip.

The physical parameters of the giant planets are often on a scale that is not resolvable with current or foreseeable computational resources. The giant planets are rapidly rotating and have low viscosity with an estimated Ekman number of $E =\sim 10^{-16}$ based on the molecular viscosity (Gastine et al., 2014). An estimate for the Ekman number based on turbulent viscosity gives $E =\sim 10^{-9}$ (Jones, 2007). This is much smaller than the lowest $E = 3 \times 10^{-6}$ used in high resolution studies (Heimpel et al., 2016) and $E = 10^{-4}$ used in this study. Lower Ekman numbers are increasingly difficult to resolve. This is because the resolution required to resolve the thickness of the Ekman boundary layer is proportional to the square root of the Ekman number. The modest Ekman number used in this study also allows us to explore a range of other parameters. The larger viscosity relative to the viscosity of a planet requires a larger Ra to force the convection to a state

of nonlinear saturation. The Prandtl number $Pr = 1$ is of similar order to estimates for the giant planets and matches previous research (Gastine and Wicht, 2012; Gastine et al., 2014). The polytropic index $m = 2$ gives a temperature structure that is comparable to planets. The radius ratio for a planet is determined by the depth of the molecular layer below which the flow is slowed down by magnetic breaking from the Lorentz force. This depth has been estimated to be $0.96R_J$ and $0.86R_S$ for Jupiter and Saturn respectively by matching the Ohmic dissipation to the planets luminosity (Liu et al., 2008). The radius ratio $\eta = 0.60$ is used in this study to avoid numerical difficulties associated with thin shells and to match previous anelastic studies (Gastine and Wicht, 2012), which we use for a basis of comparison. (We note that in a spherical shell, because the length scale is nondimensionalized according to the shell thickness $d = r_o - r_i = 1$, a shell with a larger radius ratio r_i/r_o has a larger volume and therefore requires higher resolution). The expected density stratification from a radius of $r = 0.95R_J$ to the 1 bar level is $N_\rho = 7.1$ for Jupiter (Nettelmann et al., 2008), similar to the largest $N_\rho = 7$ used in this study, however over a different radius ratio. The density contrast from $r_i = 0.60R_J$ to the 1 bar pressure level would require $N_\rho = 9.48$ which is higher than numerically feasible. However the density changes rapidly towards the outer boundary and our largest density stratification covers more than 99% of the molecular shell.

The mechanical boundary conditions employed are free-slip for both the inner and outer boundaries. This is realistic for the outer boundary of a planet which would be a free surface. However for the inner boundary Lorentz forces would slow the flow making no slip boundary conditions more physical. We use a free-slip inner boundary because a no-slip inner boundary retards the generation of zonal jets (Aurnou and Olson, 2001; Aurnou and Heimpel, 2004). Constant entropy gradient boundary conditions are used over constant entropy difference because they allow for the conductive background to grade into neutral

buoyancy. To improve the computational running time some of the simulations with a large Rayleigh number employ two-fold or four-fold symmetry in the azimuthal direction. This may affect the solution at higher latitudes and cause the flow to be more axisymmetric.

2.2 Onset of convection

The Rayleigh number Ra determines if the flow of heat is dominated by convection ($Ra > Ra_c$) or if it is dominated by conduction ($Ra < Ra_c$). Below the critical Rayleigh number fluid motion is damped for all modes. The critical Rayleigh number Ra_c is the Ra above which the first mode becomes unstable and grows. This creates linear convection cells with the same wavenumber as the mode. For anelastic simulations the wavenumber and location of the first mode changes dramatically with increasing density stratification. It is useful to consider a depth dependent Rayleigh number for these cases:

$$\mathcal{R}(r) = \frac{g(r)\beta(r)}{g_o\beta_i} Ra^*. \tag{2.1}$$

where $\beta(r) = ds_c/dr$ is the background conductive entropy gradient with s_c obtained from the conductive solution of the energy equation (1.20):

$$\nabla \cdot (\bar{\rho}\bar{T}\nabla s_c) = -H\bar{\rho}\bar{T}. \tag{2.2}$$

For constant entropy boundary conditions we use $H = 0$. For entropy gradient boundary conditions H is set to balance the entropy flux such that the model does not heat up over time.

The radial dependence of $\mathcal{R}$ is shown in figure 2.1 over a range of density stratifications for the two types of boundary conditions. The top shows the background state for constant entropy boundary conditions used in earlier anelastic studies (Gastine and Wicht, 2012).

In the near Boussisnesq state the onset of convection starts at the inner boundary where $\mathcal{R}$ is the largest. Increasing to moderate density stratification the onset of convection moves towards the outer boundary where the fluid is the least dense. There is an exponential increase in $\mathcal{R}$ as the density stratification is increased because ds_c/dr is inversely proportional to $\bar{\rho}\bar{T}$ and$\bar{\rho}$ decreases exponentially with radius Gastine and Wicht (2012). This makes for the convection to be the strongest where the density is the lowest which is very difficult to resolve. The dashed line shows the background for $N_\rho = 7$ that was not explored in the previous studies for reasons of resolution. The bottom shows the background state for constant entropy gradient boundary conditions with heat sinks to balance the entropy gradient. The entropy gradient is scaled according to the lower boundary and is set to be neutral on the surface. For all of the cases of increasing density stratification the maximum of $\mathcal{R}$ is maintained on the inner boundary and consequentially convection is forced the strongest there. The outer boundary is forced weakly where the density stratification is the strongest which allows for a larger density contrast to be resolved.

The critical Rayleigh number Ra_c and the wavenumber of convection cells near onset are shown in table 2.1 for both boundary conditions over a range of density stratifications. The critical Rayleigh number and near onset wavenumber were found by trial and error. Analytic results are available for a full sphere in the Boussinesq case (Busse, 1970), but none are available for the compressible spherical shell case . For the constant entropy boundary conditions there is a increase in the wavenumber of the convection cells with increasing density stratification. This corresponds to migration of the onset of convection from the inner to the outer boundary and from larger scale to smaller scale flow structures. For the constant entropy gradient boundary conditions with heat sinks there is an increase in near onset wavenumber with density stratification. However, it does not increase as rapidly when the convection is confined to the inner boundary. Increasing the density stratification

N_ρ	Ra_{crit}	m_{crit}
Constant Entropy Gradient Boundary		
10^{-2}	3.266×10^5	20
3	8.692×10^5	42
5	1.098×10^6	46
7	1.195×10^6	47
Constant Entropy Boundary		
10^{-2}	1.739×10^5	21
1	5.175×10^5	34
2	1.141×10^6	53
3	1.529×10^6	72
4	1.852×10^6	83
5	2.341×10^6	93

Table 2.1: Critical Rayleigh number and near onset wavenumber for increasing density stratification. The constant entropy gradient boundary conditions use heat sinks to balance the flux and prevent the system from heating up over time. Constant entropy values are from Gastine and Wicht (2012). The entropy gradient boundary conditions maintain a similar number of convection cells for strongly stratified systems. The number of convection cells increases rapidly with density stratification for the constant entropy boundary conditions.

further does not change the critical Rayleigh number or the wavenumber drastically and they may become independent of further density stratification.

The radial component of the velocity in an equatorial cross section is shown in figure 2.2 for several different cases. As the density stratification is increased from the Boussinesq case the convection cells become narrower and the wavenumber increases. The radial velocity increases with the density stratification however the radial extent of the convection cells remains relatively constant. For the constant entropy boundary conditions case the wavenumber and velocity scale increase dramatically with density stratification. As the density stratification is increased the convection cells migrate from the inner boundary to the outer boundary.

N_ρ	Ra	Ra/Ra_{crit}	Resolution	Symmetry
10^{-2}	3.430×10^5	1.05	49x128	1
10^{-2}	3.590×10^5	1.10	49x128	1
10^{-2}	4.083×10^5	1.25	49x128	1
10^{-2}	4.899×10^5	1.50	49x128	1
10^{-2}	5.716×10^5	1.75	49x128	1
10^{-2}	6.532×10^5	2.00	49x128	1
10^{-2}	1.306×10^6	4.00	49x128	1
10^{-2}	2.613×10^6	8.00	49x256	1
10^{-2}	5.226×10^6	16.00	97x256	1
10^{-2}	1.045×10^7	32.00	97x256	1
3	9.130×10^5	1.05	49x192	1
3	9.560×10^5	1.10	49x192	1
3	1.087×10^6	1.25	97x192	1
3	1.304×10^6	1.50	97x192	1
3	1.521×10^6	1.75	97x192	1
3	1.738×10^6	2.00	97x192	1
3	3.477×10^6	4.00	97x192	1
3	6.954×10^6	8.00	97x256	1
3	1.391×10^7	16.00	97x256	1
3	2.781×10^7	32.00	97x256	1
5	1.150×10^6	1.05	49x192	1
5	1.210×10^6	1.10	49x192	1
5	1.373×10^6	1.25	97x256	1
5	1.674×10^6	1.50	97x256	1
5	1.922×10^6	1.75	97x256	1
5	2.196×10^6	2.00	97x256	1
5	4.392×10^6	4.00	97x256	1
5	6.588×10^6	6.00	145x384	2
5	8.784×10^6	8.00	145x384	2
5	1.757×10^7	16.00	193x384	4
5	3.514×10^7	32.00	193x384	4
7	1.255×10^6	1.05	145x256	1
7	1.315×10^6	1.10	145x256	1
7	1.494×10^6	1.25	145x256	2
7	1.793×10^6	1.50	145x256	2
7	2.091×10^6	1.75	145x256	2
7	3.000×10^6	2.51	145x256	2
7	6.000×10^6	5.02	193x256	2
7	1.200×10^7	10.04	385x384	2
7	1.800×10^7	15.06	385x384	2

N_ρ	Ra	Ra/Ra_{crit}	Resolution	Symmetry
7	2.400×10^7	20.08	385x512	4
7	3.000×10^7	25.10	385x512	4
Constant Entropy Boundary				
5	2.580×10^6	1.10	97x256	1
5	4.900×10^6	2.09	97x256	1
5	9.800×10^6	4.19	97x256	1
5	1.470×10^7	6.00	145x512	4
5	2.000×10^7	8.54	145x512	4
5	4.000×10^7	17.09	145x512	4
5	8.000×10^7	34.17	145x512	4

Table 2.2: List of numerical simulations examining the effects of density stratification as the strength of convection is increased. Resolution is given as N_r x N_θ. Azimuthal grid points are given by $N_\phi = 2N_\theta$/Symmetry and the maximum degree of spherical harmonic expansion is $l_{max} = 2N_\theta/3$.

2.3 Convective Regimes

Increasing the Rayleigh number from near critical causes the flow to move from a linear regime to a more turbulent and time dependent flow. Convective regimes have been well documented for convection under the Boussinesq approximation (Christensen, 2001) (Grote and Busse, 2001). For weakly supercritical Rayleigh number the flow is in stationary convection cells that drift azimuthally with the zonal flow being weaker or of similar magnitude to the poloidal flow. Increasing the Rayleigh number further up to 10 - 20 times critical causes the kinetic energy to be time dependent and dominated by the zonal flow component. The flow is characterized by quasiperiodic bursts in the poloidal component of the flow that feeds the zonal flow, which decays exponentially between cycles. In the third regime the Rayleigh number is more than 20 times critical and the zonal flow is more dominant. The energy becomes more chaotic in time, however there are still some periodic

bursts in energy.

The regimes of anelastic convection over a range of density stratifications with increasing Rayleigh number have also been documented (Gastine and Wicht, 2012). Near the onset of convection the energy is constant in time and the flow is in linear convection cells. Increasing the Rayleigh number slightly still close to convection causes the flow to oscillate regularly in amplitude while maintaining the convective cells. The next regime is chaotic flow and the energy is dominated by the zonal flow. The following regime is oscillatory in both poloidal and toroidal energy dominated by the toroidal flow. The final regime is nonlinear with no sizeable oscillations. In general increasing the density stratification caused the convective regimes to tighten or even disappear.

Figures 2.3 - 2.6 show the time evolution of the kinetic energy for the poloidal and toroidal components of the flow for increasing density stratification and Rayleigh number. Near the onset of convection the kinetic energy becomes independent of time and the flow is in linear convection cells attached to the inner boundary that are advected azimuthally. For the near Boussinesq case the toroidal component of the kinetic energy is larger than the poloidal component near the onset of convection. However, increasing the density stratification causes the poloidal component to dominate initially. As the Rayleigh number is further increased the toroidal component dominates in all cases and the poloidal component begins to experience quasi periodic behaviour. In the third regime the the energy becomes chaotic for both components. In the final regime there are periodic bursts of convection followed by relaxation in both components of the energy.

The convective regimes for all runs are shown in figure 2.7. The relaxation oscillation regime was not observed for the near Boussinesq case however it may emerge at higher Rayleigh numbers. In general the convective regimes tightened as the density stratification was increased similar to observed for previous research (Gastine and Wicht, 2012).

The convective regimes observed here were similar to those observed in previous anelastic models however the second chaotic regime was not observed for the strongly convecting systems. It is suggested that in the previously observed second chaotic regime the flow scale becomes increasingly small-scale disrupting the convective columns in the axis of rotation (Gastine and Wicht, 2012). The buoyantly neutral outer boundary reduces the vigor of convection near the outer boundary, which may explain the missing regime.

2.4 Zonal Flow Development

In deep models of the zonal flow on Jupiter and Saturn the flow is driven by convection in a spherical shell. In a strongly rotating Boussinesq convective system with low viscosity the Taylor-Proudman theorem approximately holds. In a system with density stratification the Taylor-Proudman theorem holds for the azimuthal component of the velocity u_ϕ. However the other components of the flow and the entropy will not be z-independent (Jones and Kuzanyan, 2009). The convection cells are organized parallel to the axis of rotation. However near the boundaries the geometry violates Taylor-Proudman theorem, and a secondary flow develops. The convection cells are tilted by the boundary curvature causing a net transport of momentum that feeds the zonal flow. The zonal flow further tilts the convection cells creating a positive feedback until the internal viscous stresses balance the Reynolds stresses (Vasavada and Showman, 2005). In a strongly rotating system the effects of the boundary geometry are quantified by the β-parameter. The scale at which the zonal flow saturates and the energy cascade ceases is the Rhines length, which is inversely proportional to β (Rhines, 1975). In shallow models the zonal flow is confined to a spherical surface and β_s is proportional to the gradient of the coriolis parameter $f = 2\Omega sin\lambda$ with latitude λ. For spherical shell models there is a topographical β-parameter $\beta_h = \frac{2\Omega}{h}\frac{dh}{ds}$, with cylindrical radius s, that is dependent on the gradient of the fluid column height

(Heimpel and Aurnou, 2007).

The development of zonal flow is shown in figures 2.8 and 2.9 for a range of density stratifications and Rayleigh numbers for constant entropy gradient boundary conditions with a neutral outer boundary. The zonal flow initially develops as a prograde equatorial jet inside the tangent cylinder. The first retrograde jet develops on the border of the tangent cylinder and is typically weaker then the equatorial jet except in the near Boussinesq case. At low Rayleigh numbers the flow is fairly axisymmetric as predicted by Taylor-Proudman theory. As the Rayleigh number is increased the equatorial jet begins to saturate and flow begins to develop inside of the tangent cylinder. Increasing the density stratification tends to increase the velocity scale of the flow and causes the first retrograde jet to disconnect from the tangent cylinder.

The zonal flow development for increasing Rayleigh number at a moderate density contrast is shown for constant entropy boundaries in figure 2.10. In contrast to cases with the entropy gradient boundary conditions, the prograde equatorial jet initially develops in a thin region at the outer boundary. As the strength of convection is increased the equatorial jet becomes deeper and the first retrograde jet begins to develop. Higher latitudinal jets start to develop with increasing Ra. However, turbulent structure also develops near the outer boundary.

The surface zonal flow for a strongly stratified convecting system is shown in figure 2.11 for both boundary conditions. For the constant entropy boundary conditions there is a strong prograde jet in the equatorial region. At polar latitudes the flow is smaller scale and there are no well defined jets. The equatorial jet for the entropy gradient boundary conditions is much more smooth. At polar latitudes there is a well developed retrograde jet. The flow is larger scale overall because the depth dependent Rayleigh number grades to buoyantly neutral for this case.

The radial vorticity at the north pole is shown for the two boundary conditions in figure 2.12. For the case with the constant entropy boundary conditions there is strong vorticity at the surface. However it is mostly small scale structure and there are not large scale vortices. For the constant entropy gradient boundary conditions the vorticity scale is near planetary vorticity $\omega_p = 2\Omega$. There is strong anticyclonic vorticity that is bordered by thin cyclonic filaments. Towards the equator the vortices become more elongated.

2.5 Dynamic Stability

The depth dependent Rayleigh number, given by equation (2.1), measures the strength of convection based on the radial derivative of the conductive entropy. We can consider the time and space dependence of convective (thermal) stability by considering a variable stability parameter Υ that is proportional to the radial derivative of the full entropy:

$$\Upsilon(r,\theta,\phi,t) = \frac{g(r)}{c_p\Omega^2}\frac{\partial s(r,\theta,\phi,t)}{\partial r}. \tag{2.3}$$

If the radial derivative of the entropy $\partial s/\partial r$ is negative the system is convective and Υ expresses the strength of the convection. If $\partial s/\partial r$ is positive the system is thermally stably stratified. Although the system has neutral thermal stability at the outer boundary in the conductive background the relaxation oscillations tend to stabilize on average when the poloidal kinetic energy is at a maximum. Figure 2.14 shows the radial thermal stability at the minimum and maximum of the poloidal energy component. The time-averaged thermal stability over several relaxation oscillations is also shown. The outer boundary is heated by thermal convection which causes a local inversion of the entropy gradient that creates thermal stability. Constant entropy difference boundary conditions create a thermal boundary layer near the surface that prevents this kind of inverted entropy gradient. The

azimuthally averaged stability is shown in figure 2.13 for a strongly convecting stratified run. Over a time average there is neutral to weak thermal stability mostly near the poles. The strongest thermal stability occurs near the outer boundary inside the tangent cylinder when the system is convecting strongly.

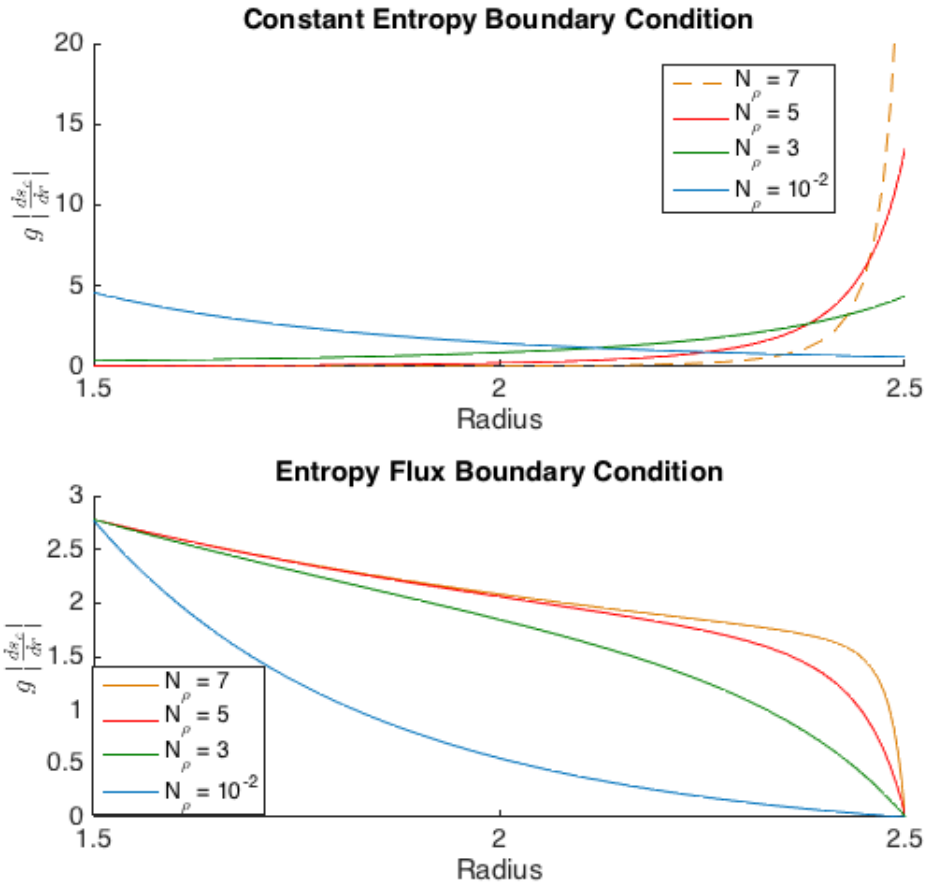

Figure 2.1: Comparison for $g|ds_c/dr|$ for density stratifications $N_\rho = [10^{-2}, 3, 5, 7]$ for simulations with constant entropy boundary conditions with no sinks (top) and with constant entropy gradient boundary condition with sinks (bottom). The dashed line shows the background state for $N_\rho = 7$ that was not explored in previous studies and peaks at $g|ds_c/dr| = 37$ at the outer boundary. For the strongly stratified flow there is a sharp increase in the entropy gradient required to maintain the constant difference. The entropy gradient boundary conditions use a volumetric entropy sink so that the model does not heat up over time.

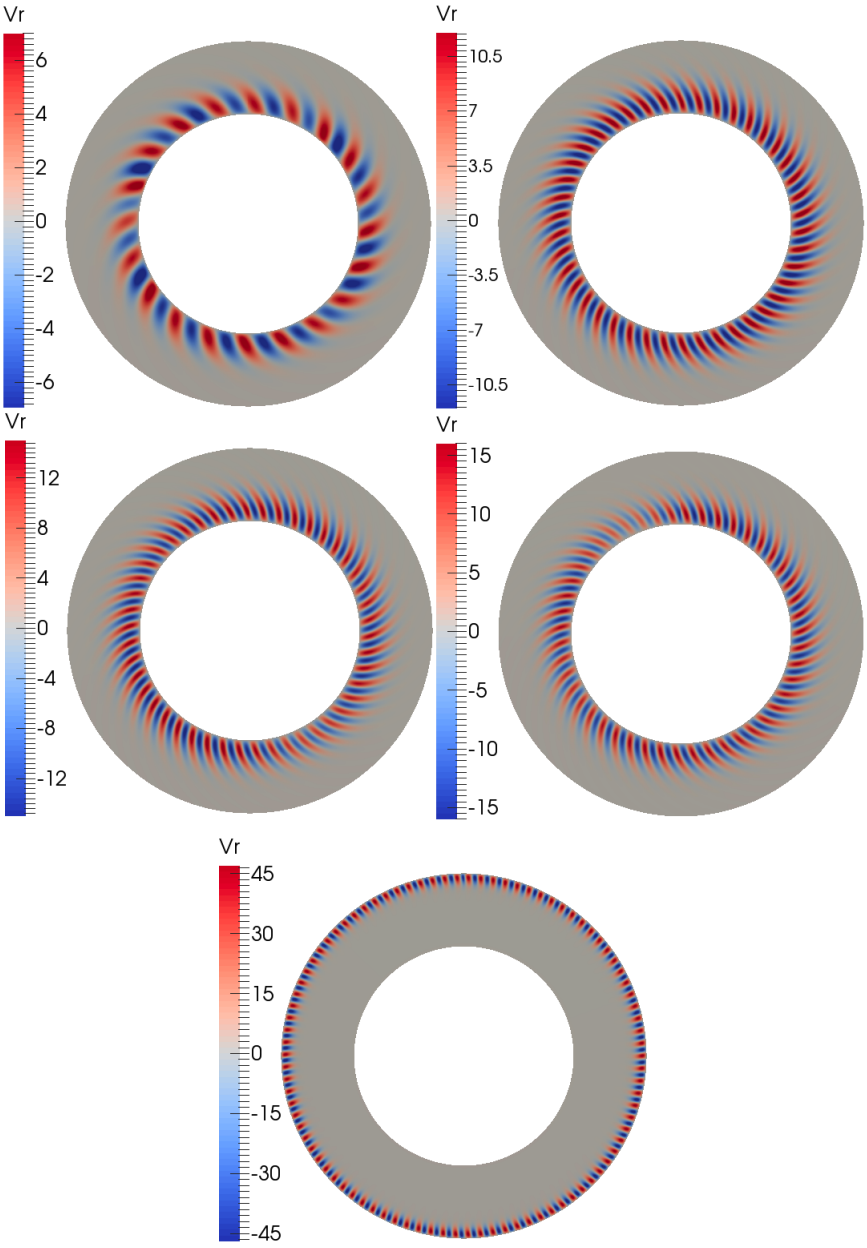

Figure 2.2: Equatorial cross section of radial velocity v_r near the onset of convection $Ra \sim 1.10 Ra_c$. top left to middle right: $N_\rho = 10^{-2}$, 3, 5, 7 for entropy gradient boundaries. Bottom: $N_\rho = 5$ for constant entropy boundaries. Velocities are scaled in terms of the Reynolds Number. For the constant entropy gradient boundary conditions convection cells remain attached to the inner boundary and their wavenumber increases with density stratification ($m \propto N_\rho$). For strongly stratified constant entropy boundary conditions the onset of convection moves to the outer boundary.

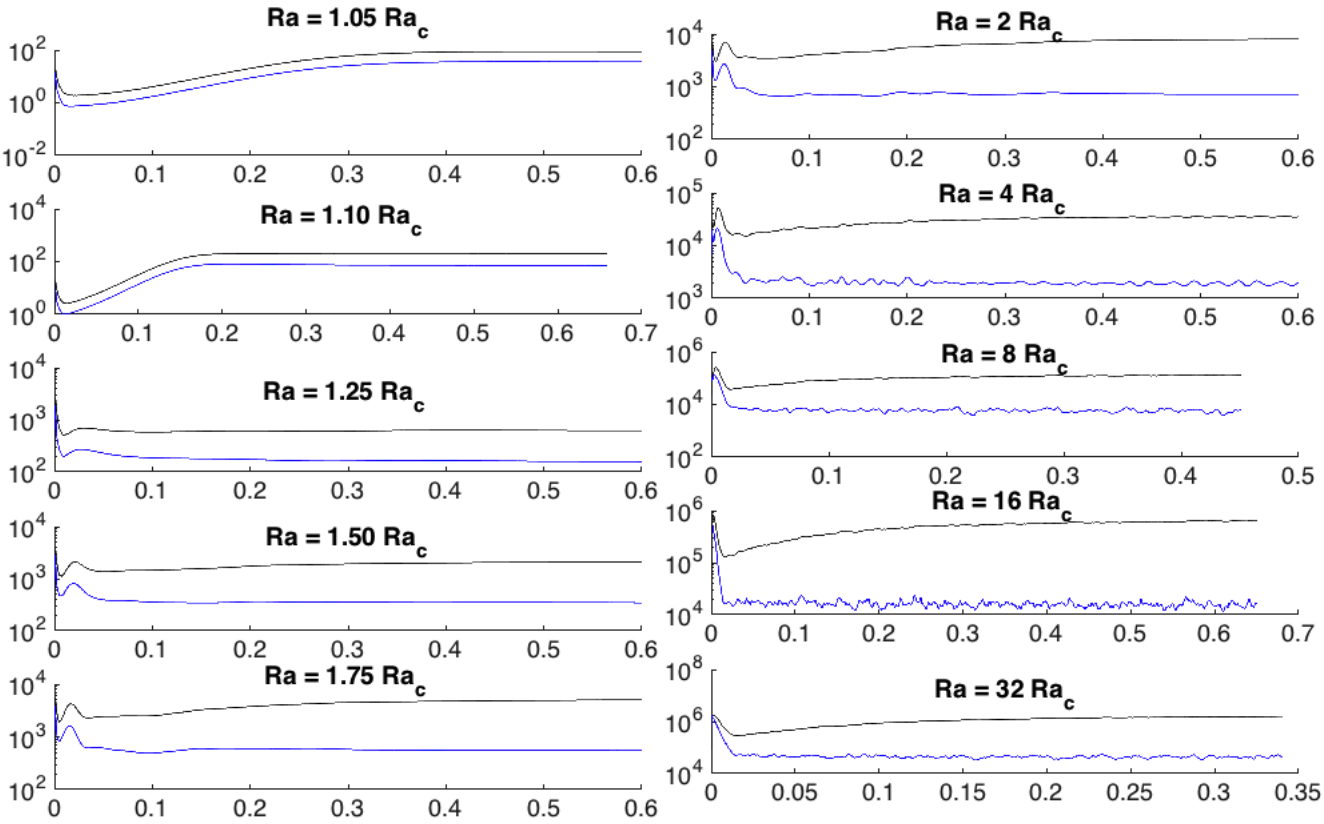

Figure 2.3: Kinetic energy time series for runs with density stratification $N_\rho = 10^{-2}$. The black represents the toroidal component of the flow and the blue represents the poloidal component of the flow.

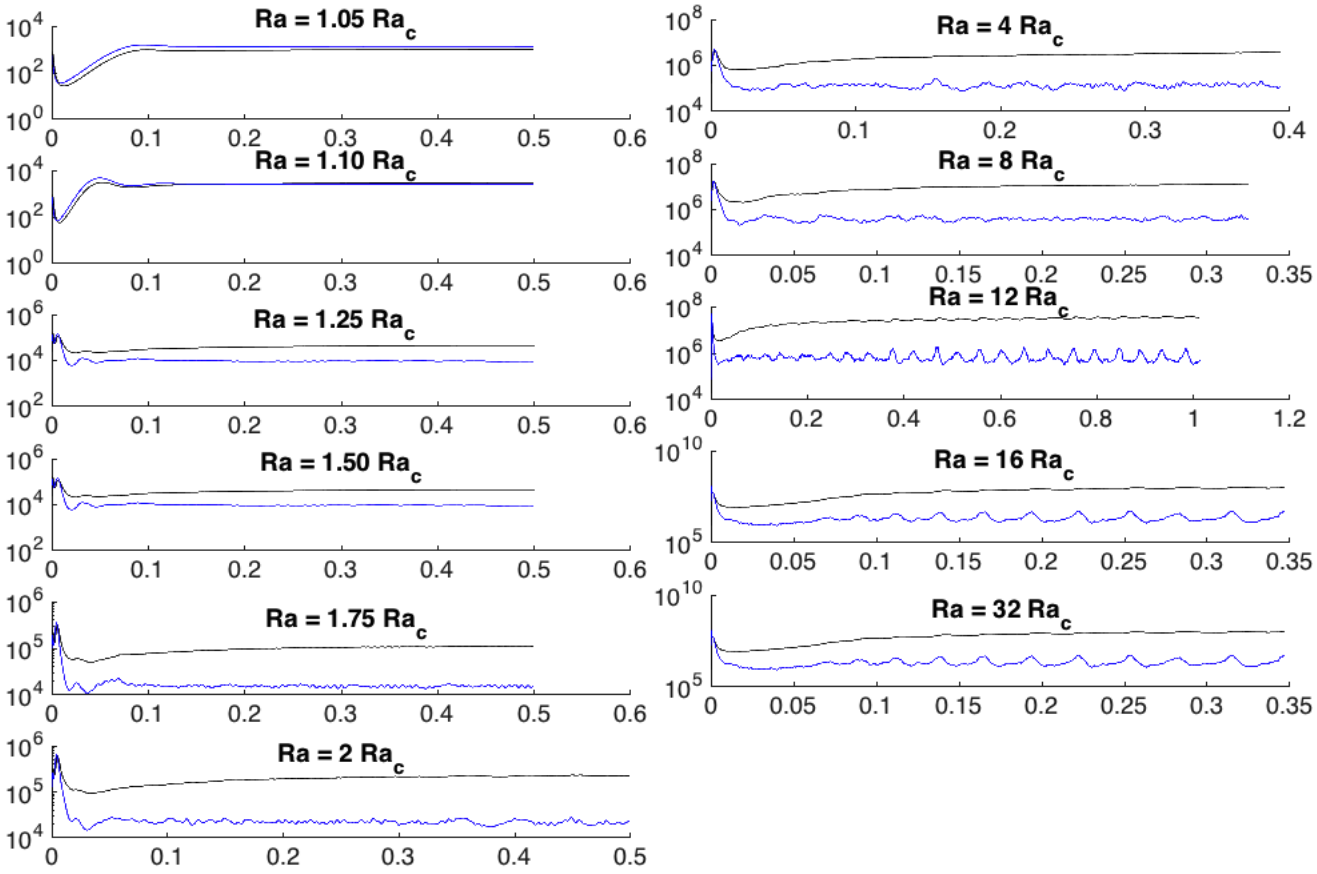

Figure 2.4: Kinetic energy time series for runs with density stratification $N_\rho = 3$. The black represents the toroidal component of the flow and the blue represents the poloidal component of the flow.

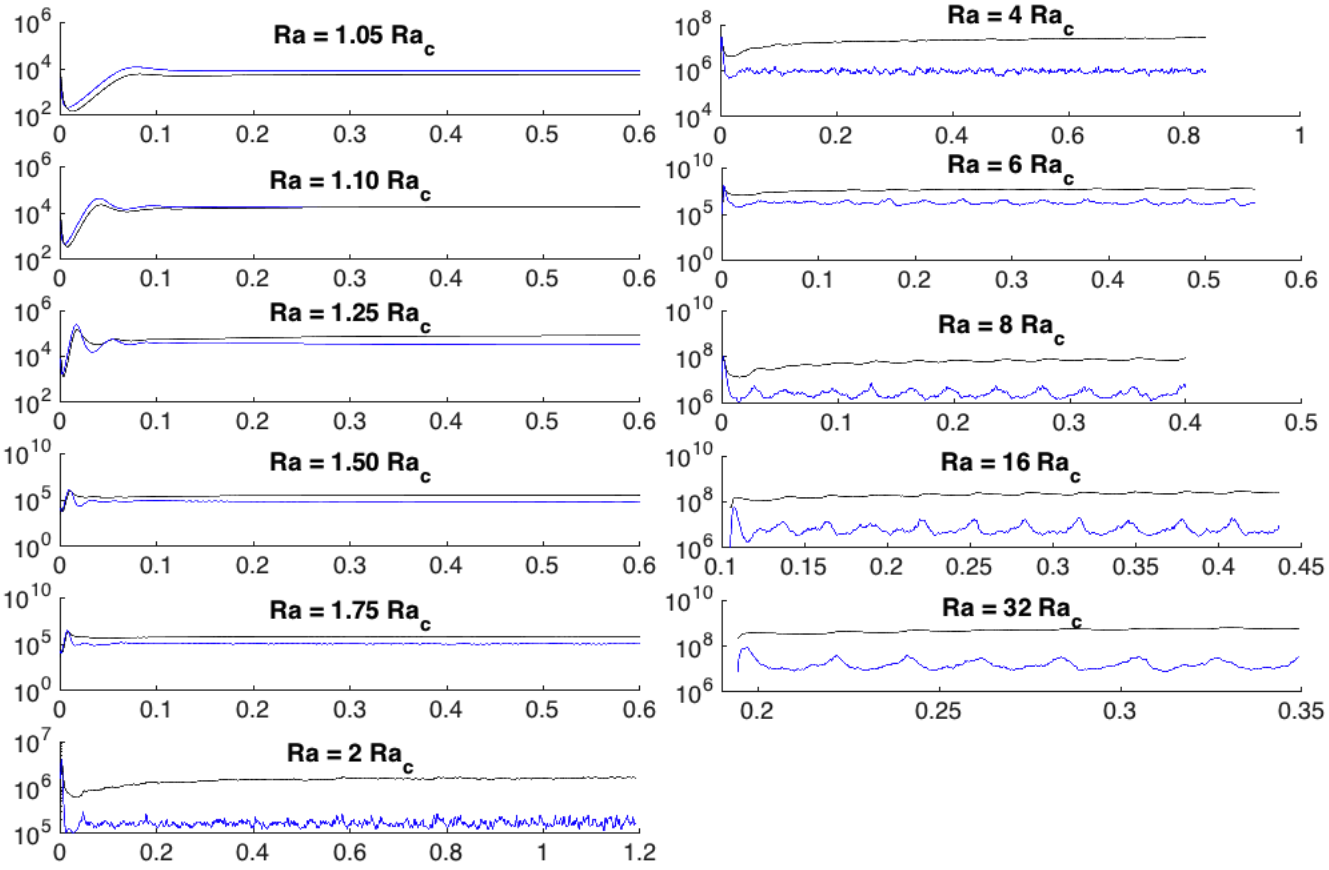

Figure 2.5: Kinetic energy time series for runs with density stratification $N_\rho = 5$. The black represents the toroidal component of the flow and the blue represents the poloidal component of the flow.

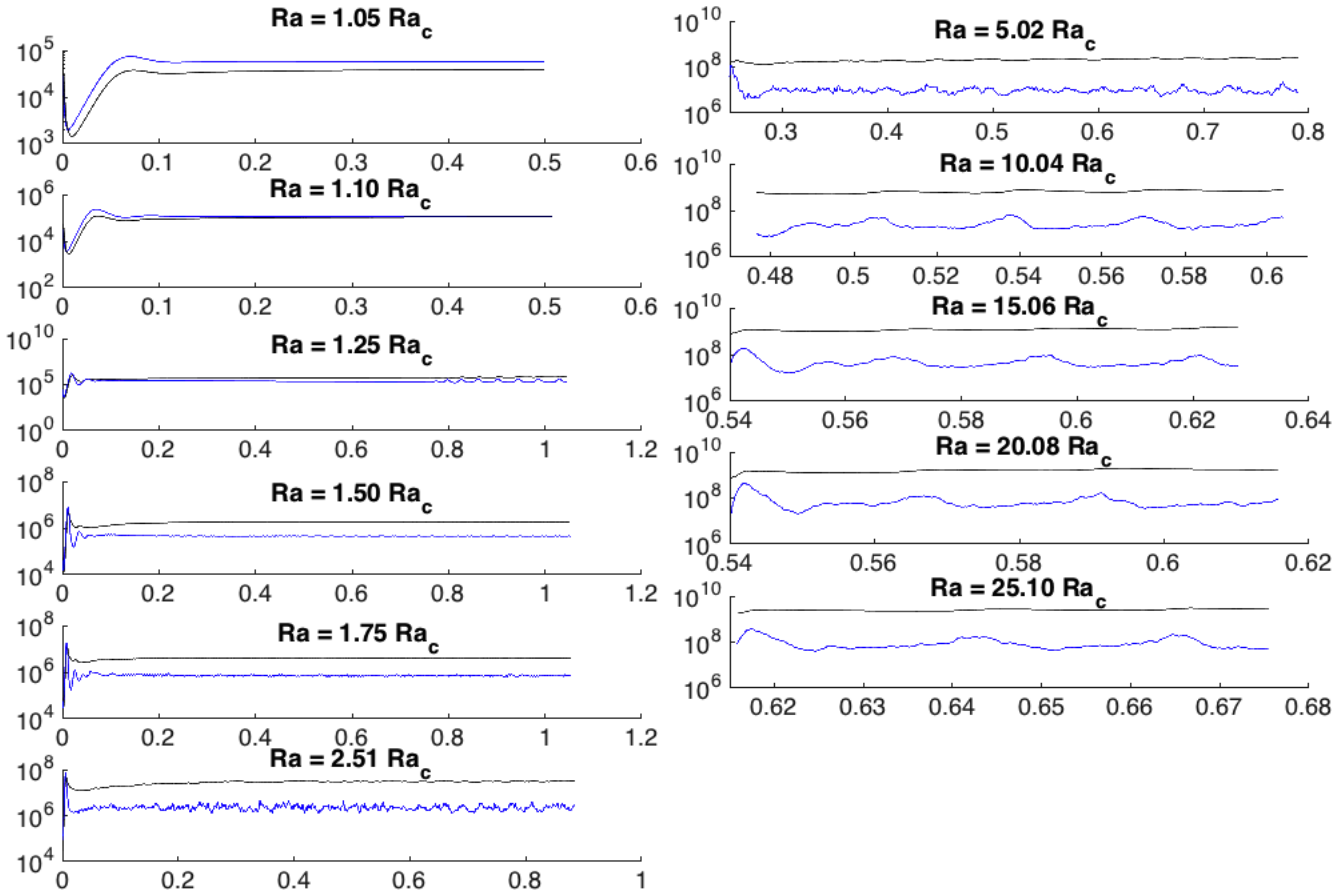

Figure 2.6: Kinetic energy time series for runs with density stratification $N_\rho = 7$. The black represents the toroidal component of the flow and the blue represents the poloidal component of the flow.

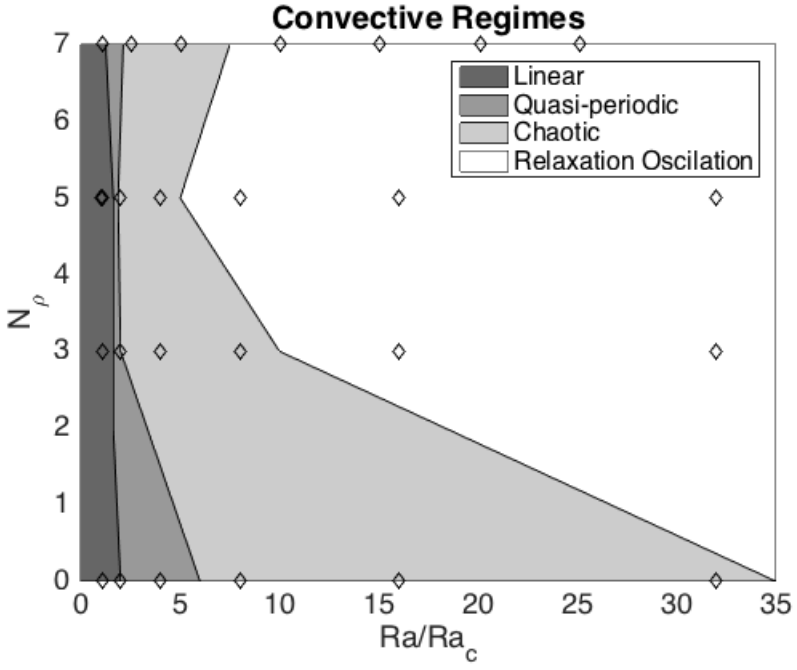

Figure 2.7: Regime diagram for the modes of convection for numerical simulations over a range of density stratification and increasing Rayleigh number. As the density stratification is increased the spacing between modes becomes more narrow. The second chaotic regime observed in previous anelastic studies (Gastine and Wicht, 2012) was not found here.

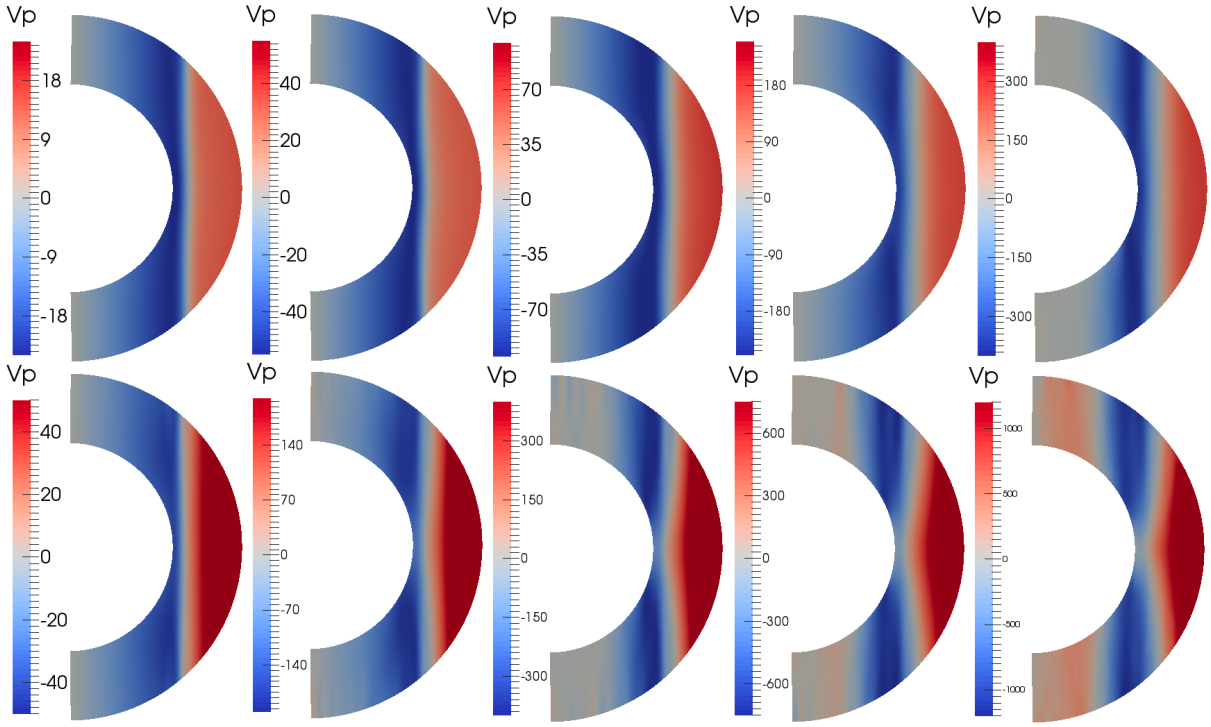

Figure 2.8: Azimuthally averaged zonal velocity for models with increasing Rayleigh Number (left to right) and increasing density stratification (10^{-2} top, 3 bottom) scaled according to the Reynolds number.

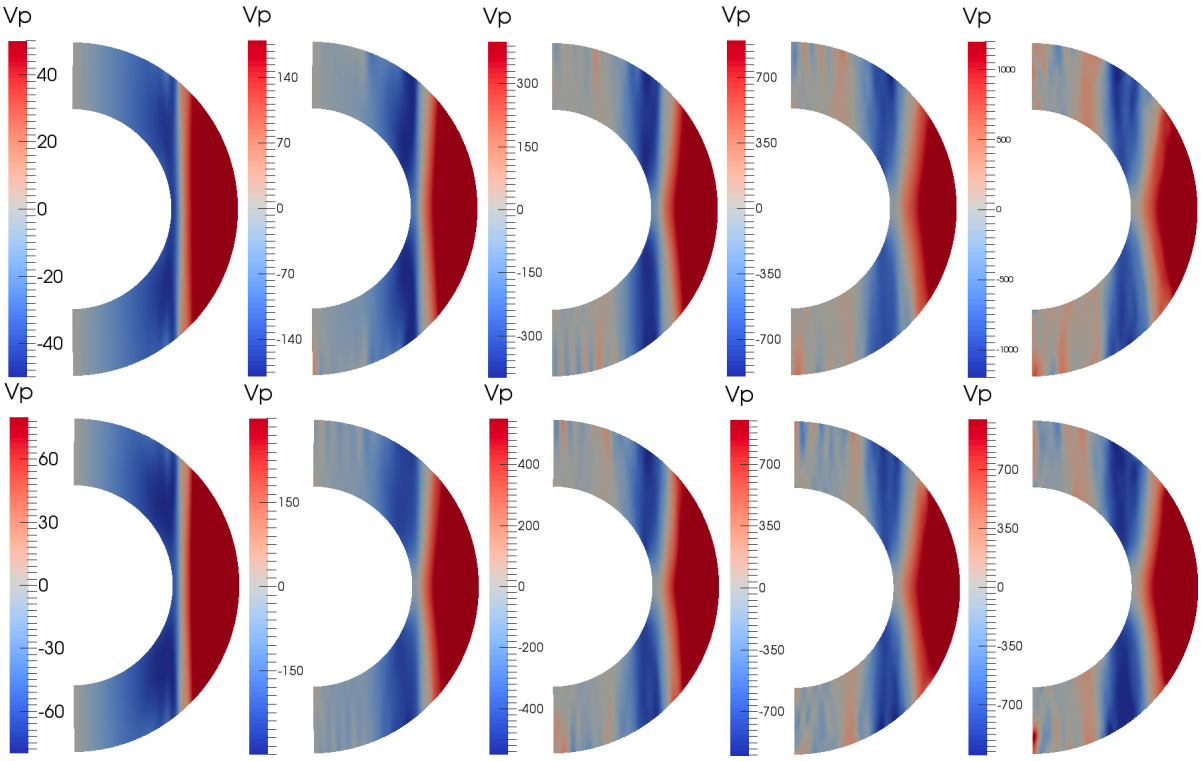

Figure 2.9: Azimuthally averaged zonal velocity for models with increasing Rayleigh Number (left to right) and increasing density stratification (5 top, 3 bottom) scaled according to the Reynolds number.

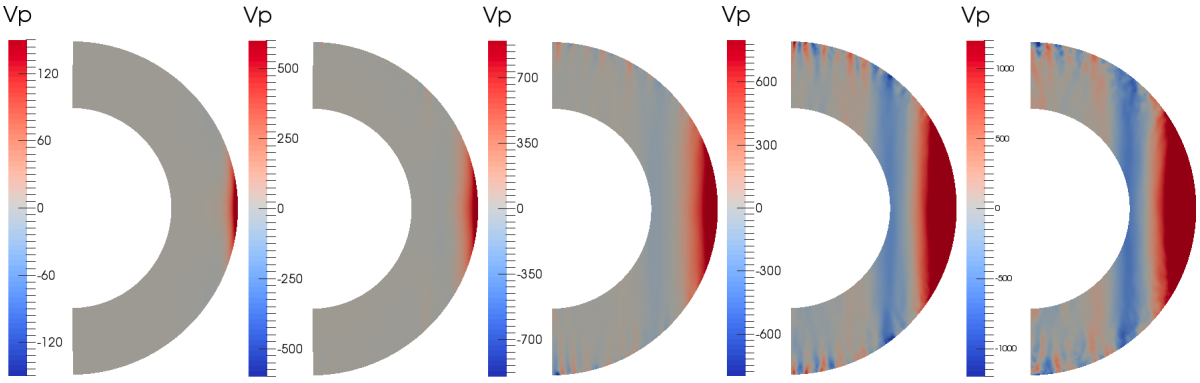

Figure 2.10: Azimuthally averaged zonal velocity for strongly stratified constant entropy boundary conditions. The flow near the outer boundary is increasingly small scale because the large entropy flux required at the outer boundary to maintain a constant entropy difference. Velocities are scaled according to the Reynolds number.

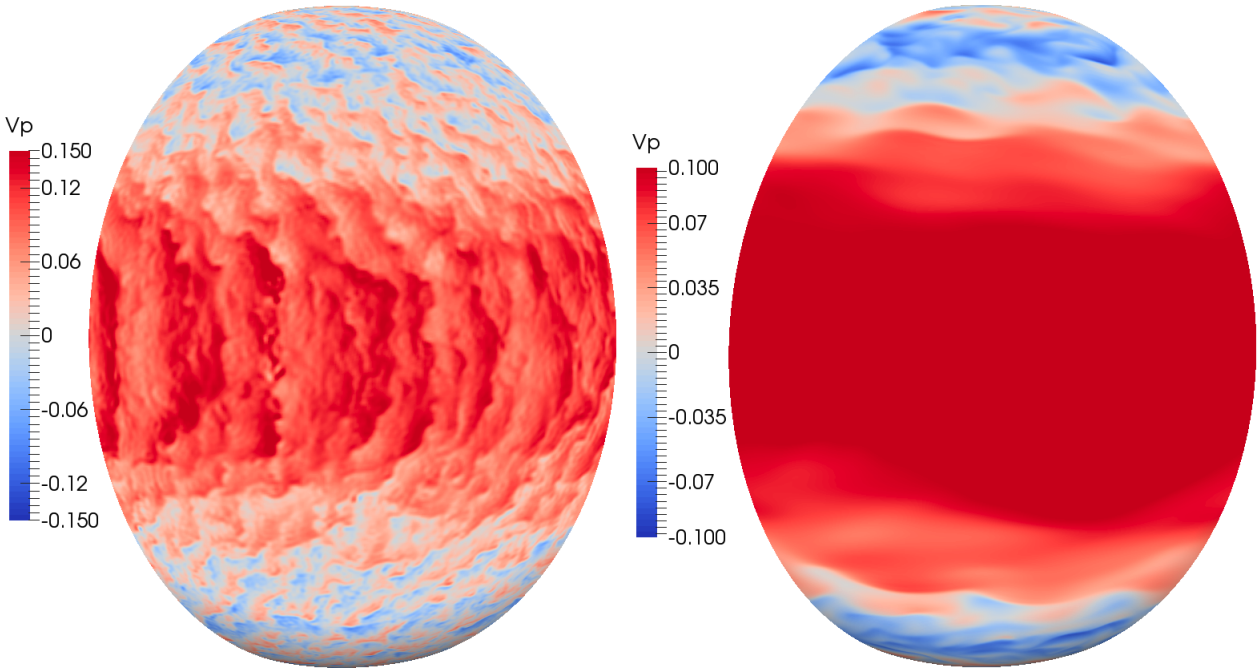

Figure 2.11: Comparison of the azimuthal velocity for a strongly convecting system. $N_\rho = 5$ with constant entropy boundary conditions (left) and $N_\rho = 7$ with constant entropy gradient boundary conditions (right). Velocities are scaled in terms of the Rossby number.

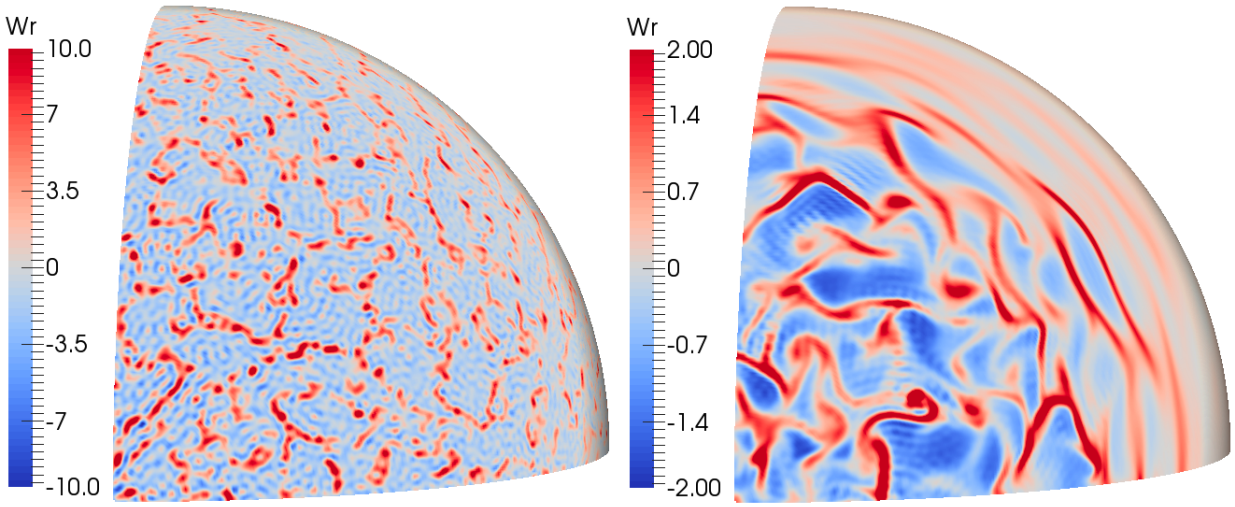

Figure 2.12: Comparison of the radial vorticity (north polar view) for a strongly convecting system. $N_\rho = 5$ with constant entropy boundary conditions (left) and $N_\rho = 7$ with constant entropy gradient boundary conditions (right).

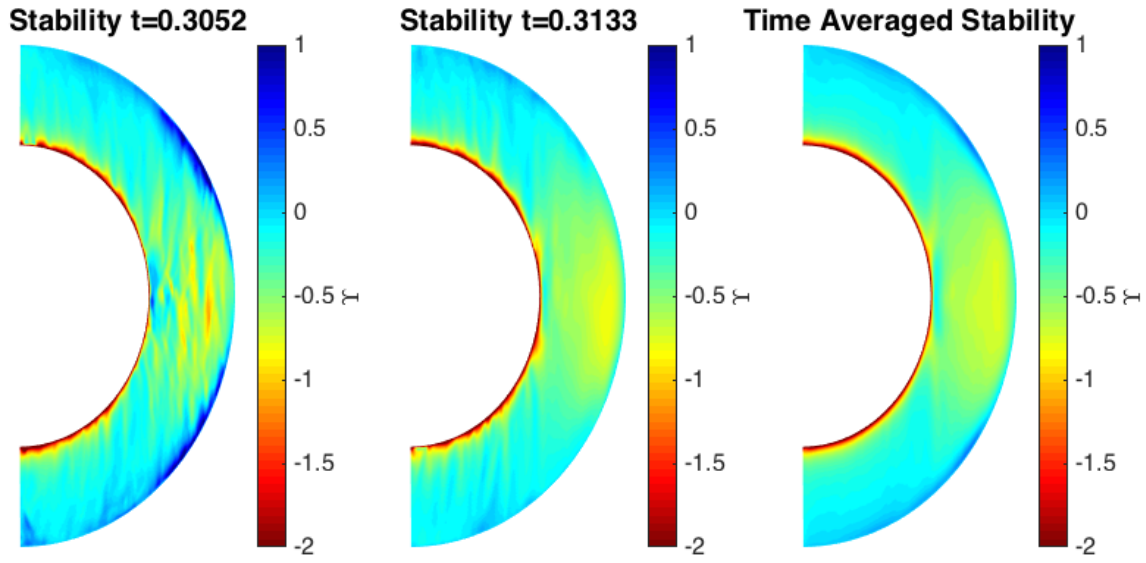

Figure 2.13: Azimuthally averaged stability Υ for strongly convecting run with $N_\rho = 5$ and $Ra = 32Ra_c$. The stability peaks at a maximum in poloidal energy (left) and is weakest at a minimum (middle). Time averaged thermal stability is shown to the right.

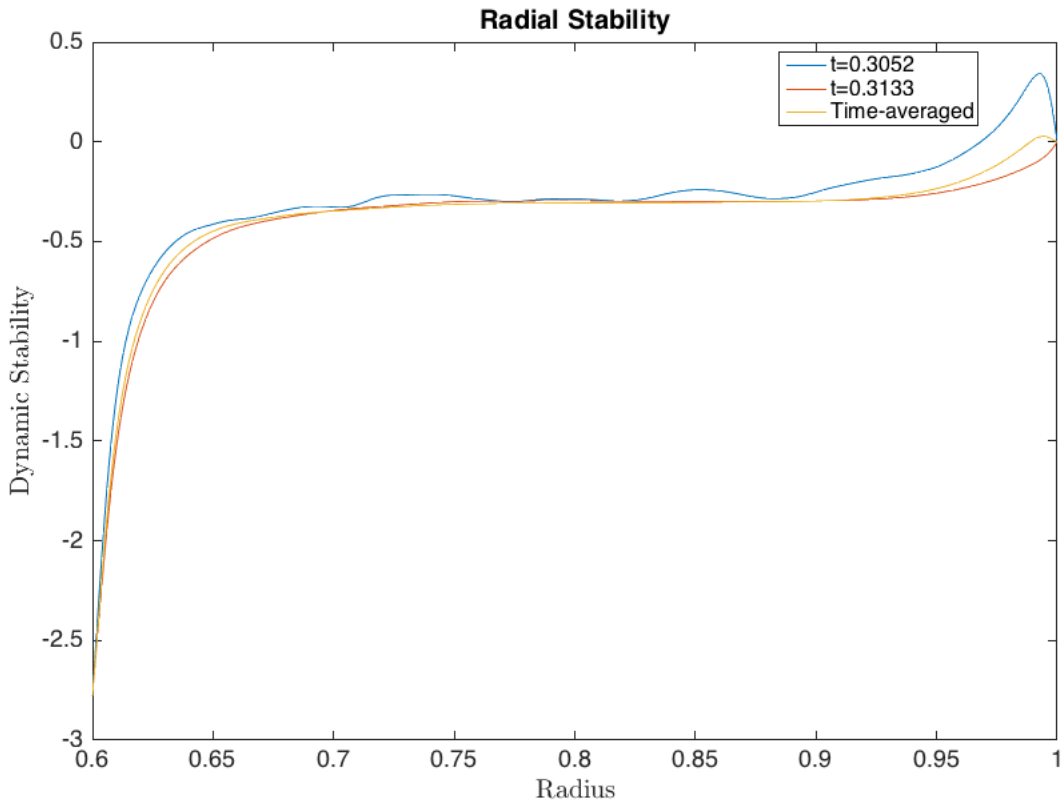

Figure 2.14: Radial stability Υ for strongly convecting run with $N_\rho = 5$ and $Ra = 32Ra_c$. Blue shows the stability at a peak of a poloidal kinetic energy. Red shows the stability when the poloidal kinetic energy is at a minimum. Yellow shows the time averaged thermal stability over several oscillations.

Chapter 3

Nonhomogeneous Boundary Conditions

The effects of a thermal plume from the deep interior on a thin molecular shell can be modelled as an entropy flux perturbation on the lower boundary. There are many parameters that will affect the solution, such as the amplitude of the perturbation, how narrow or wide it is, the latitudinal offset of the source, and the strength of the convection of the background fluid. The system is strongly rotating such that the convection promoted by the source is constrained along the axis of rotation. The constant entropy gradient boundary conditions allow for the formation of an entropy hotspot axially above the source. This can create an inversion of the temperature gradient axially which leads to dynamic convective stability. This localized region of stability allows for generation of vortices.

3.1 Numerical Modelling

The equations of anelastic convection are solved numerically by the pseudospectral code MagIC which allows for nonhomogeneous thermal boundary conditions. The boundary

conditions must be provided in spectral space and therefore a spherical harmonic transformation must be applied to the function chosen for the boundary. To model a convective plume from the deep interior we choose a Gaussian shaped perturbation superimposed on a constant gradient background:

$$f(\theta,\phi) = A\exp\left(-\frac{(\theta-\theta_0)^2}{2\sigma^2} - \frac{(\phi-\phi_0)^2}{2\sigma^2}\right) + B. \tag{3.1}$$

Where A is the amplitude of the plume, B is the background gradient, θ_0 is the latitude offset, ϕ_0 is the longitudinal offset, and σ is a measure of the standard deviation of the gaussian function in terms of colatitude. The conversion between σ and the offset in degrees is shown in table 3.1. This model requires that the plume is sufficiently far away from the pole or narrow such that the Gaussian function decays away from the pole. For a source that is placed directly on the pole there is no offset in θ and it becomes a 1d Gaussian function that is independent of ϕ:

$$f(\theta,\phi) = A\exp\left(-\frac{\theta^2}{2\sigma^2}\right). \tag{3.2}$$

The Gaussian shaped perturbations are useful because there are analytic integrals that can relate the width and amplitude of the anomaly to the flux of entropy emitted

$$V = \int_0^{2\pi}\int_0^{\pi}\left(A\exp\left(-\frac{(\theta-\theta_0)^2}{2\sigma^2} - \frac{(\phi-\phi_0)^2}{2\sigma^2}\right) + B\right)d\theta d\phi = 2\pi A\sigma^2 + 4\pi^2 B. \tag{3.3}$$

For the polar source because there is no offset in θ it is half of a Gaussian function that peaks in amplitude at $\theta = 0$. This has an analytic integral given by:

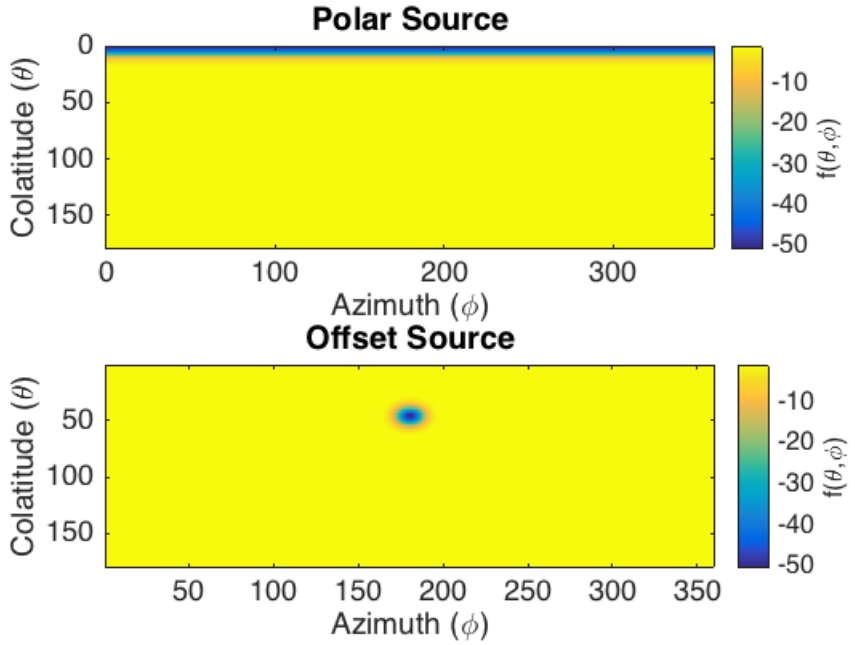

Figure 3.1: Sample of two different anomalies in spherical coordinate space for the cases of an anomaly at the north pole and an anomaly offset by 30 degrees. For both of these cases $\sigma = 0.10$. The polar source is modelled using a 1d Gaussian function and the offset source is modelled using a 2d Gaussian function.

$$V = \int_0^{2\pi} \int_0^{\pi} \left(A \exp\left(-\frac{\theta^2}{2\sigma^2} \right) + B \right) d\theta d\phi = \pi\sqrt{2\pi} A\sigma + 4\pi^2 B. \tag{3.4}$$

In both of these equations the left term in the right hand side represents the entropy flux attributed to the source and the right terms represents the entropy flux associated with the background. In order to apply these functions as the boundary condition we must first find the spherical harmonic coefficients for them. The spherical harmonic functions and the forward transform into spherical harmonic coefficients are detailed in section (1.4.2). The grid space representation for two potential sources is shown in figures 3.1 for a polar source and a source offset by 30 degrees. This shows the difference in the representation as a 1d

Width (σ)	Width ($^\circ$)
0.071	15
0.100	22
0.150	32

Table 3.1: Relation between the Gaussian function standard deviation and the planetary colatitude after which 99% of the source has decayed.

Gaussian function for a source at the pole compared to a 2d Gaussian function for a source away from the pole. The amplitude of the spherical harmonic coefficients in spectral space is shown in figure 3.2 for the two cases up to degree 50. For both cases the amplitude of the coefficients tend to zero before reaching the maximum degree. This means that enough coefficients were used to fully resolve the perturbation. The polar source requires far less coefficients than the offset source because the symmetry requires only zonal harmonics of the form Y_l^0. In general a narrow source with a high amplitude will require a higher maximum degree of expansion.

Introducing an entropy flux source on the lower boundary will alter the Rayleigh number locally near the source. We define a modified Rayleigh number for the source Ra_s^* based on the amplitude of the source scaled by the modified Rayleigh number Ra^*. The background gradient on the inner boundary is set to -1 so that the flux based Rayleigh number is identical to the standard Rayleigh number. This gives Ra_s^* as

$$Ra_s^* = ARa^* = A\frac{g_0}{c_p\Omega^2}. \tag{3.5}$$

In general the amplitude of the source will be strongly convective relative to the background Rayleigh number.

While the spherical harmonic functions are natural functions for modeling physical equations on a sphere the inhomogeneous coverage in the polar region can cause problems

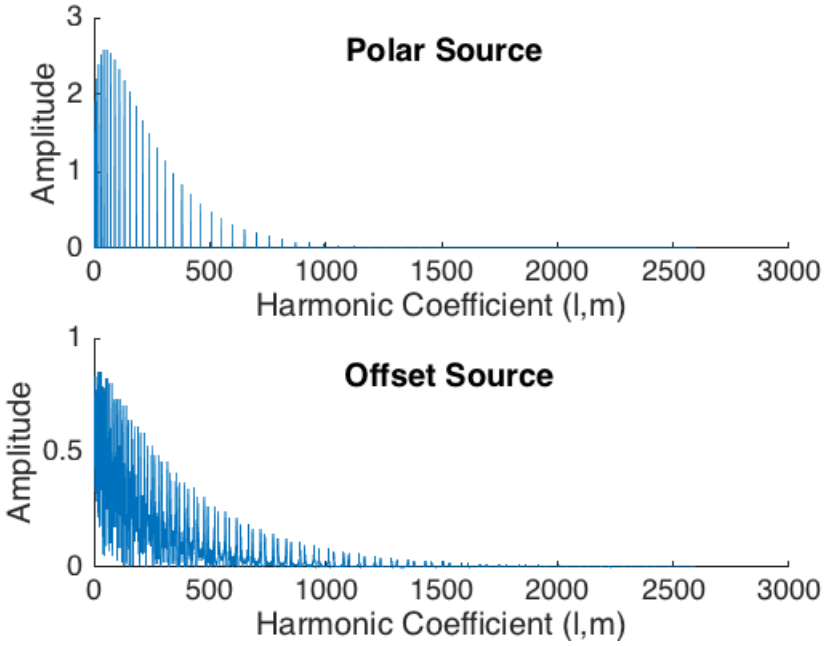

Figure 3.2: Spherical harmonic coefficients of a polar source (top) and a offset source (bottom) up to a degree 50. The maximum degree should be chosen such that the coefficients tend to zero to ensure that the source is modelled completely.

when modelling features at the pole. Towards the pole the spherical mesh becomes much more dense azimuthally while the latitudinal spacing remains constant causing the cells become highly elongated quadrilaterals. For a full sphere $N_\phi = 2N_\theta$ so that the resolution is isotropic in the equatorial region. Other models for geodynamo simulations have solved the problem of nonhomogeneous grid spacing by employing a yin-yang grid that reuses the low latitude band to cover the polar region (Kageyama and Yoshida, 2005). This method resolves the problems in the polar region, however it is not suitable for spectral methods and requires a finite difference method.

Case	Offset	Amplitude	Ra/Ra_c	Resolution
3.2.1	0	25	0.50	97x256
3.2.2	0	25	0.80	97x256
3.2.3	0	25	2.00	145x256
3.2.4	0	50	0.50	97x256
3.2.5	0	50	0.80	97x256
3.2.6	0	50	2.00	145x256
3.2.7	45	25	0.50	97x256
3.2.8	45	25	0.80	97x256
3.2.9	45	25	2.00	145x256
3.2.10	45	50	0.50	97x256
3.2.11	45	50	0.80	97x256
3.2.12	45	50	2.00	145x256
3.2.13	90	25	0.50	97x256
3.2.14	90	25	0.80	97x256
3.2.15	90	25	2.00	145x256
3.2.16	90	50	0.50	97x256
3.2.17	90	50	0.80	97x256
3.2.18	90	50	2.00	145x256

Table 3.2: List of numerical simulations exploring non-homogeneous boundary condition offset-amplitude-background relation. Resolution is given as N_r x N_θ. Azimuthal grid points are given by $N_\phi = 2N_\theta$ and the maximum degree of spherical harmonic expansion is $l_{max} = 2N_\theta/3$.

3.2 Effects of source offset and background Rayleigh number

The effects of an entropy flux source at the lower boundary are dependent on the latitudinal offset of the source, the amplitude of the source, and on the background Rayleigh number. The effects of a source in isolation can be considered by setting the background Rayleigh number Ra to be subcritical such that any convective motion comes from the source. The locations of the source include a polar source with an offset of $\phi_0 = 0$, a mid latitude source with an offset of $\phi_0 = 45$, and an equatorial source with an offset of $\phi_0 = 90$. For these experiments the radius ratio is taken to be $\eta = 0.60$ and the Ekman number $E = 10^{-4}$ to match the previous chapter and the density stratification is taken to be $N_\rho = 5$ for a moderate contrast that is easily resolvable.

Figure 3.3 shows the kinetic energy timeseries for the toroidal and the poloidal components of the flow for runs with an equatorial source. The toroidal component dominates the energy in all cases and it falls into the nonlinear convective regime. Systems where the background Rayleigh number was less than the critical Rayleigh number were able to drive a weak global zonal flow with the forcing of the source. When the $Ra^* > Ra_c^*$ the flow of the source and the jets developed are stronger. In general the kinetic energy profile of the flow was similar for the three different locations and is probably independent of the offset.

The stability of the flow above the anomaly is represented by the entropy gradient, as show in figure 3.4. The anomalies are strongly convective on the inner boundary. However there is a region of stability near the outer boundary to the north of the source in the $\hat{z}$ direction, and in the case of the equatorial anomaly to the south as well. The areas of dynamic stability come from an inversion on the entropy gradient associated with convection caused by the source. The surface vorticity associated with the different location of sources is shown in figure 3.5. At the outer boundary there is a hotspot associated with the convective plume. In general the source produced anticyclonic vortices shielded by a cy-

clonic filament produced at the surface. As the storms are advected away from the hotspot they dissipate viscously, until they vanish. New vortices are constantly generated at the surface above the plume. The flow is dominated by rotation, and the Taylor-Proudman theorem approximately holds even for anomalies that are locally much higher than the critical Rayleigh number ($Ra_s^* >> Ra_c^*$). Thermal convection caused by the source is aligned with the axis of rotation even with an equatorial source source where the buoyancy is perpendicular to the axis of rotation.

3.3 Effects of source width and amplitude for a polar source

The amplitude and width of the entropy flux perturbations on the lower boundary have a significant effect on the characteristic of the surface flow. The relative width of the spherical shell is also important in defining the surface flow. Here we consider a thinner spherical shell with a radius ratio $\eta = 0.80$ that is closer to planetary, which should emphasize the effects of the source. The density stratification remains at $N_\rho = 5$ and the background Rayleigh number is chosen to be nonconvective with $Ra/Ra_c = 0.40$. All of the sources in this section are polar.

The overall strength of the source can be quantified by considering the entropy flux associated with the source. The entropy flux is the integral of the source boundary and is given by equation (3.4). The time-averaged azimuthal velocity, time-averaged entropy, time-averaged vorticity, and a vorticity snapshot are shown in figures 3.6 - 3.11 over a range of increasing source width and amplitude. In general a source can produce 2-3 high latitudinal jets. In most cases there is a prograde jet at the pole flanked by a retrograde jet at lower latitude. In cases with a wide anomaly and a low source amplitude there are typically three jets. A retrograde jet at the pole, a prograde jet at a slightly lower latitude, and another retrograde jet at low latitude. There is an entropy hotspot at outer boundary

of the pole that is proportional to the width and amplitude of the perturbation on the lower boundary. The time-averaged vorticity shows cases where there is a cyclonic or anticyclonic vortex at the pole. The most narrow cases (3.3.1-3.3.6) produced a cyclonic vortex for all amplitudes examined and the vortex was generally more smooth than in wider cases. For the cases with a wider source the polar vorticity was on average anticyclonic for cases with low to mid amplitude (3.3.7-3.3.10,3.3.12). In the high amplitude case $A = 200$ there was a cyclonic polar storm for the range of widths. For the wider cases, (3.3.11,3.3.15), the cyclonic storm was wider, weaker, and had more small scale features compared to the narrow source. The vorticity snapshots show transient storms that are constantly generated by the source. These storms are typically have an anticyclonic core that is shielded with a cyclonic filament. Generating storms requires a stronger amplitude for the sources that are wider.

On Saturn a cyclonic vortex has been observed by the Cassini spacecraft at both the north and the south poles. The south polar vortex was initially observed as a polar hotspot from an Earth based telescope (Orton and Yanamandra-Fisher, 2005). High-resolution observations from Cassini showed that the storm has a nearly cloud free eye that is bordered by two cloud walls with a height of 20-70km (Dyudina et al., 2009). The northern polar vortex was observed to be similar to the southern vortex with a ring of clouds. However the northern cyclone shows a discrete cloud feature rather than a clear eye (Baines et al., 2009).

The narrow source produces a consistent cyclonic vortex similar to that which is observed for Saturn. Our results are consistent with a previous study, which suggested that the planetary vorticity gradient interacts with storms causing the cyclonic anomalies to migrate poleward and the anticyclonic anomalies to migrate towards the equator, until their magnitude equals the magnitude of the background vorticity (O'Neill et al., 2015). This

is apparently the case for the polar vortex shown in figure (3.7). Vorticity at the surface is being constantly generated by the anomaly and is distributed with cyclonic vorticity at the pole and anticyclonic vorticity at lower latitudes. Figure (3.12) shows how shielded anticyclonic vortices tend to migrate from near polar to a lower latitude. There are no constant anticyclones in the time averaged vorticity because there is a large band where they exist briefly. The storms tend to saturate with a vorticity that is near planetary. The wider sources produced anticyclonic vortices at lower latitudes when forced with a large amplitude. The maximum extent of the storms is comparable to the extent of the entropy hotspot produced. This would be within the region of stability created by the inversion of the temperature gradient caused by the hotspot. The anticyclones may be produced when convective flow from the interior diverges at the surface.

Case	Amplitude	σ	Flux	Resolution
3.3.1	25	0.071	13.98	145x384
3.3.2	50	0.071	27.96	145x384
3.3.3	75	0.071	41.93	145x384
3.3.4	100	0.071	55.91	145x384
3.3.5	150	0.071	83.87	145x384
3.3.6	200	0.071	111.82	145x576
3.3.7	20	0.10	15.75	97x256
3.3.8	50	0.10	39.37	97x256
3.3.9	100	0.10	78.75	97x256
3.3.10	150	0.10	118.12	145x256
3.3.11	200	0.10	157.50	145x384
3.3.12	50	0.15	111.82	145x256
3.3.13	100	0.15	59.06	145x256
3.3.14	150	0.15	117.18	145x384
3.3.15	200	0.15	236.24	145x384

Table 3.3: List of numerical simulations exploring non-homogeneous boundary condition amplitude-width relation. The entropy flux is the integral over the boundary and is dependent on the amplitude and width and can be used to compare narrow large amplitude sources to wide low amplitude sources. Resolution is given as N_r x N_θ. Azimuthal grid points are given by $N_\phi = 2N_\theta$ and the maximum degree of spherical harmonic expansion is $l_{max} = 3N_\theta/2$.

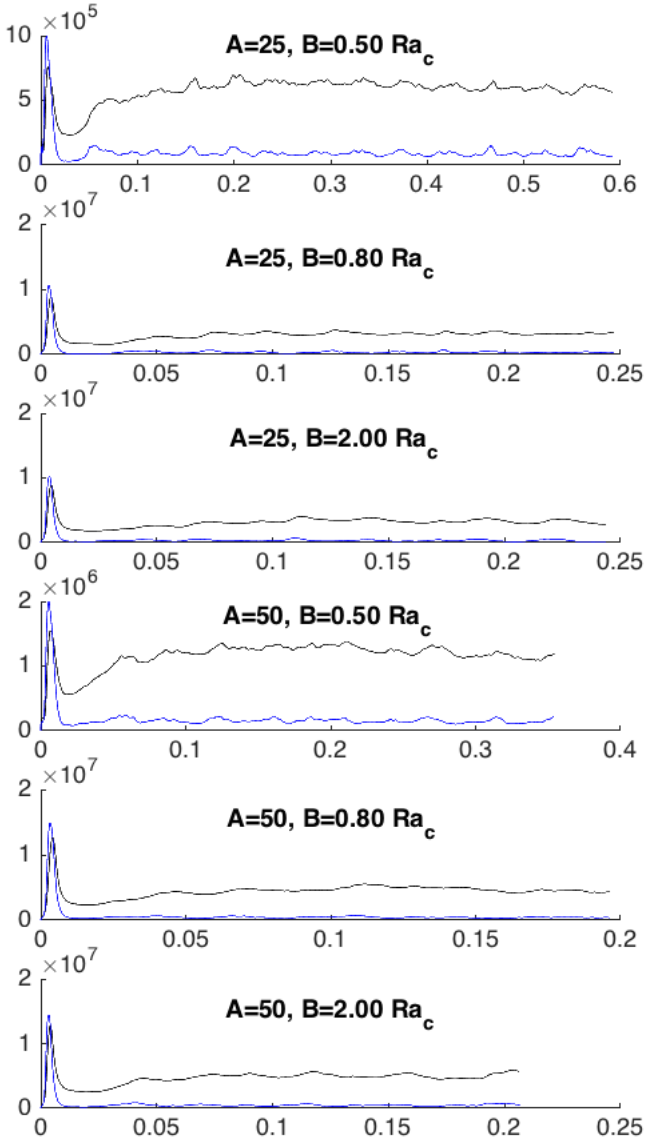

Figure 3.3: Kinetic energy timeseries for an equatorial source (offset $\phi_0 = 90°$). The energy is in the chaotic regime observed in the previous chapter. The energy timeseries was similar for the polar source and the $\phi_0 = 45$ source.

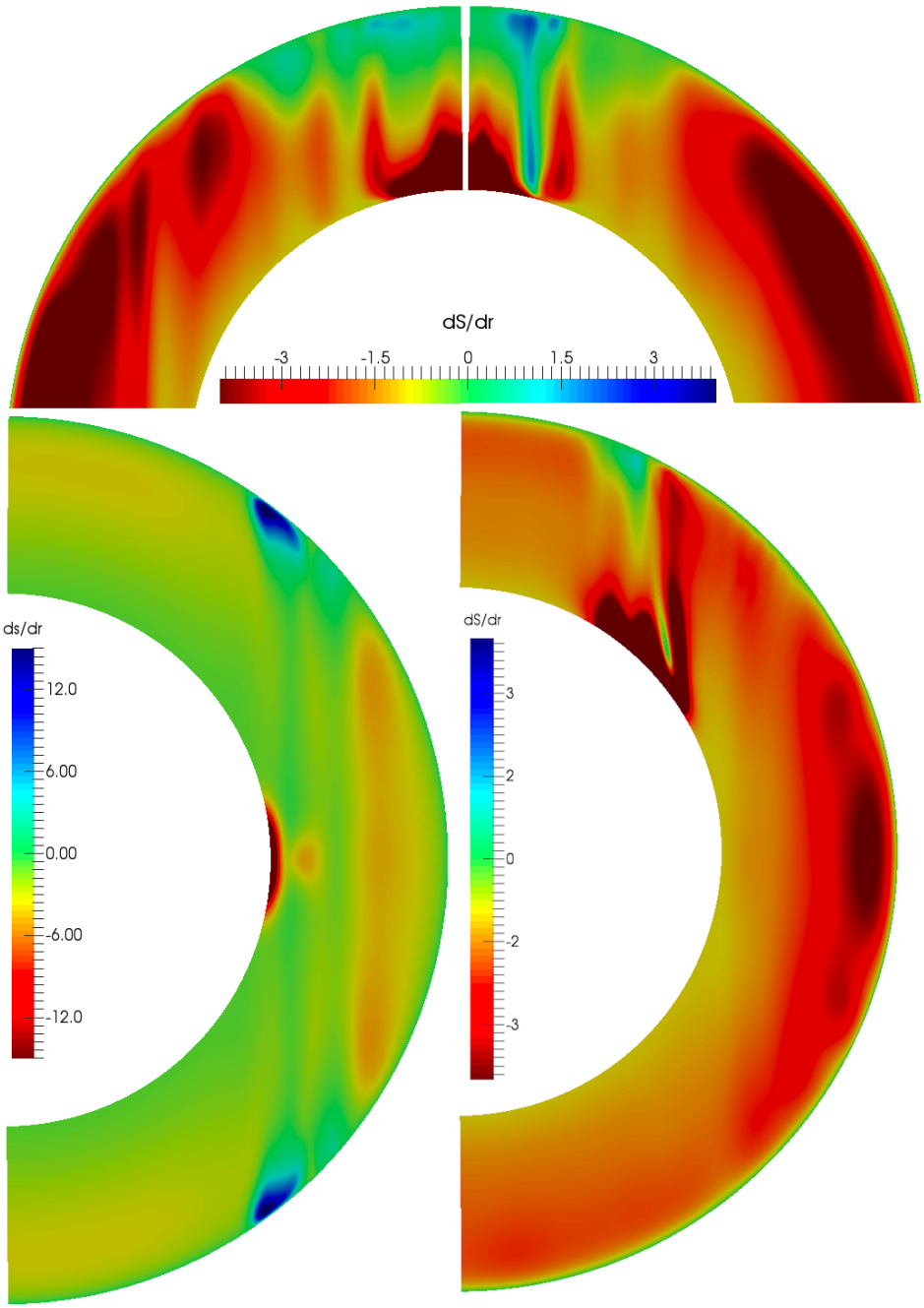

Figure 3.4: Entropy gradient for three sources of differing offset. Polar source, case 3.2.6 (top), equatorial source, case 3.2.18 (left), and 45° offset source, case 3.2.12 (right). The entropy gradient boundary condition allows for the surface to heat up causing a entropy gradient inversion that results in dynamic buoyant stability.

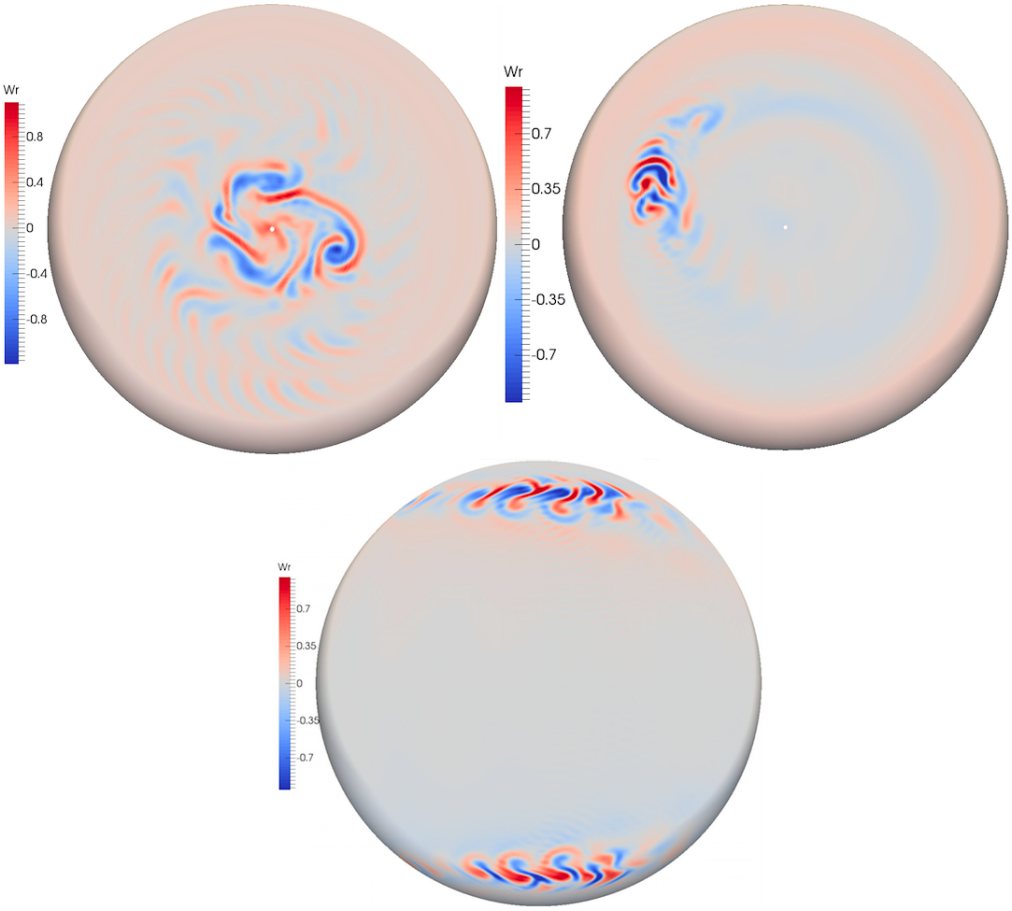

Figure 3.5: Surface radial vorticity for three sources of differing offset scaled to the planetary vorticity. Polar source, case 3.2.6 (top left), 45° offset source, case 3.2.12 (right), and equatorial source, case 3.2.18 (bottom). In the northern hemisphere anticyclonic vortices are produced with a cyclonic filament.

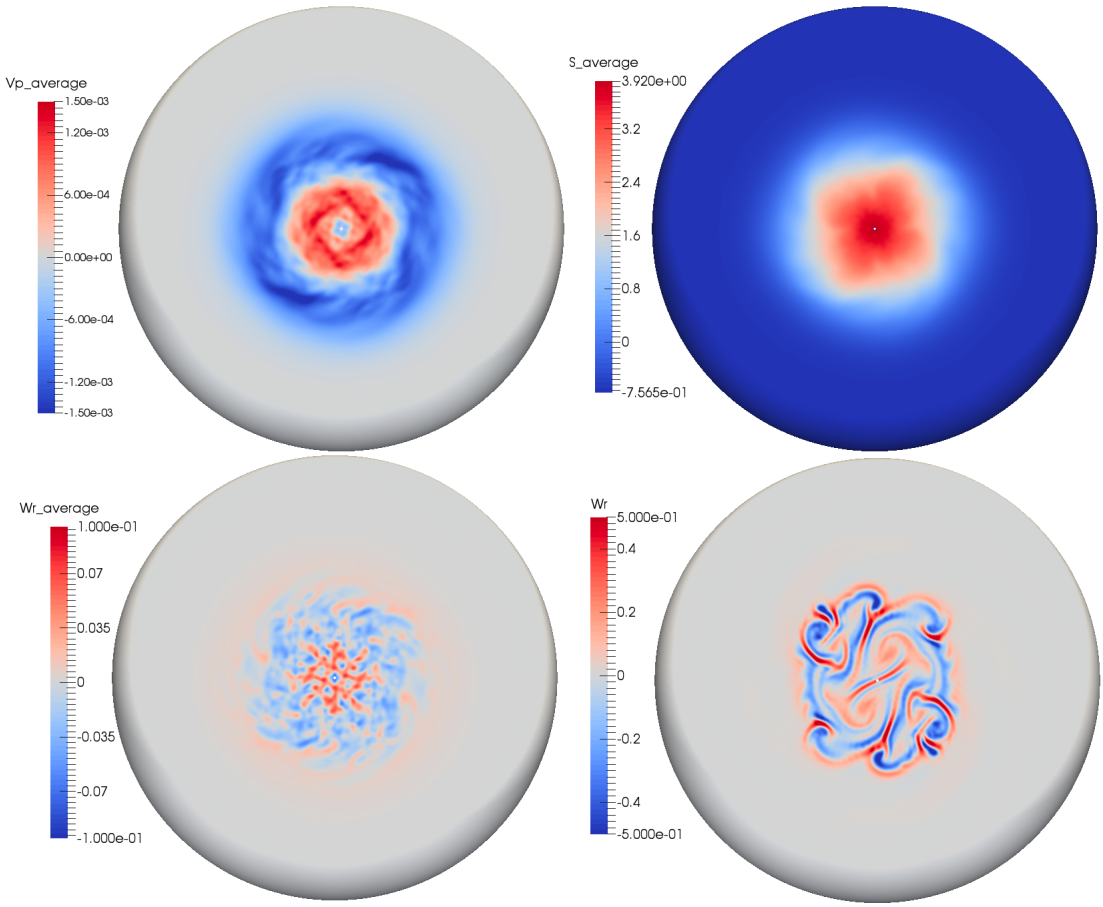

Figure 3.6: Time-averaged azimuthal velocity (top left), time-averaged entropy (top right), time-averaged radial vorticity (bottom left), and radial vorticity snapshot (bottom right) for case 3.3.2 with $\sigma = 0.071, A = 50, V = 27.96$.

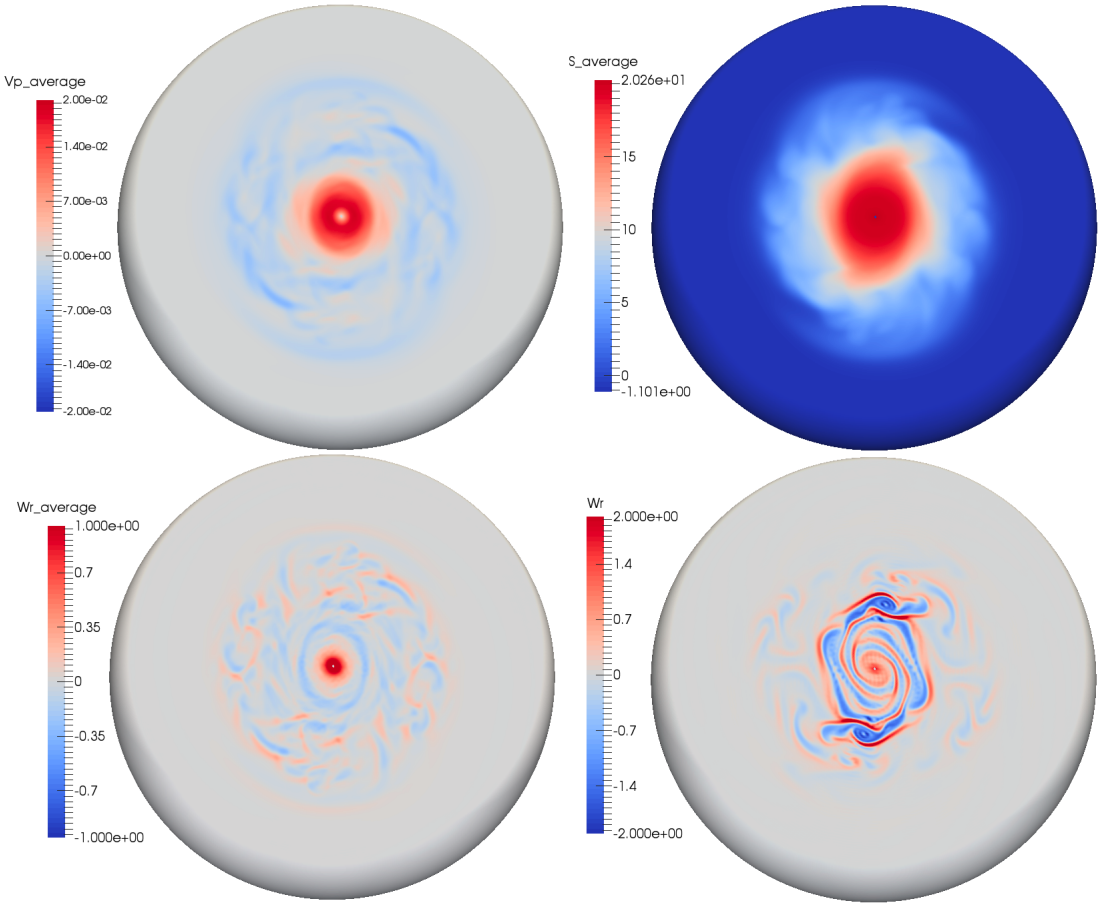

Figure 3.7: Time-averaged azimuthal velocity (top left), time-averaged entropy (top right), time-averaged radial vorticity (bottom left), and radial vorticity snapshot (bottom right) for case 3.3.6 with $\sigma = 0.071, A = 200, V = 111.82$.

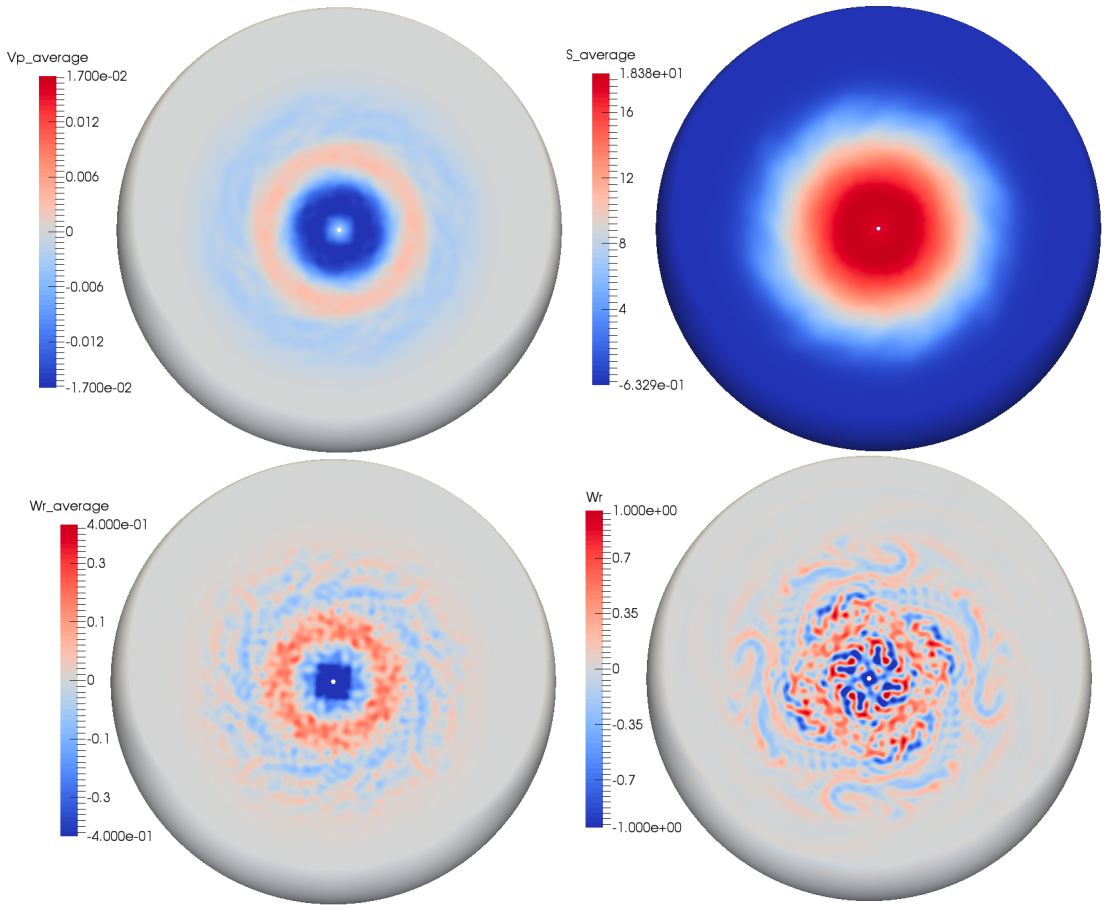

Figure 3.8: Time-averaged azimuthal velocity (top left), time-averaged entropy (top right), time-averaged radial vorticity (bottom left), and radial vorticity snapshot (bottom right) for case 3.3.10 with $\sigma = 0.10, A = 150, V = 118.12$.

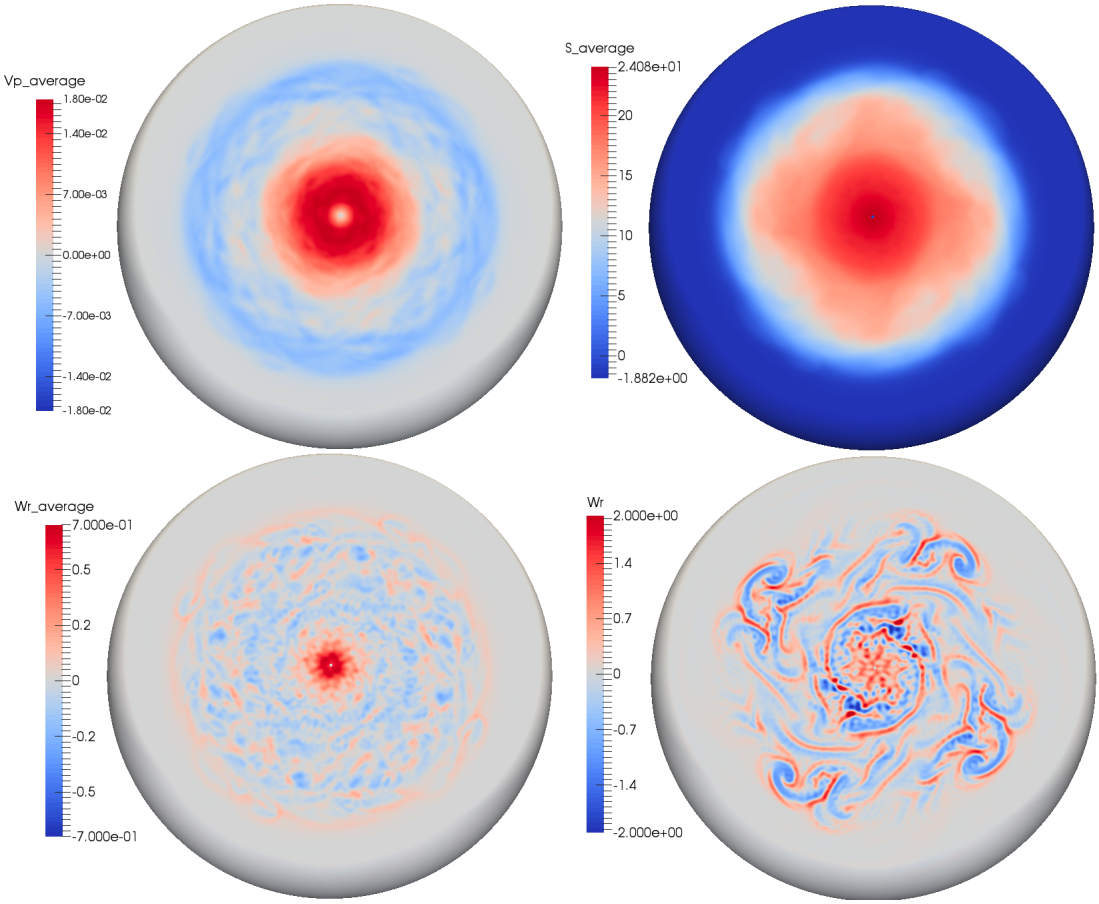

Figure 3.9: Time-averaged azimuthal velocity (top left), time-averaged entropy (top right), time-averaged radial vorticity (bottom left), and radial vorticity snapshot (bottom right) for case 3.3.11 with $\sigma = 0.10, A = 200, V = 157.50$.

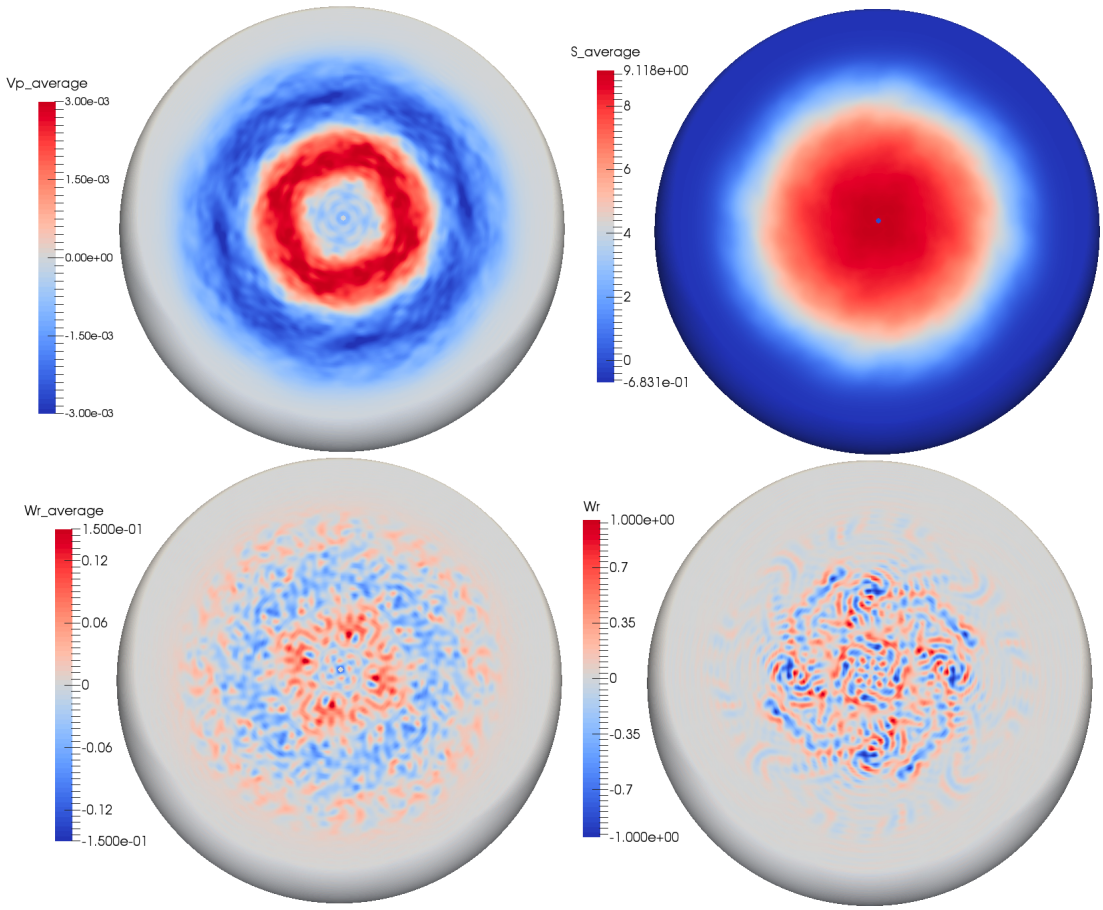

Figure 3.10: Time-averaged azimuthal velocity (top left), time-averaged entropy (top right), time-averaged radial vorticity (bottom left), and radial vorticity snapshot (bottom right) for case 3.3.12 with $\sigma = 0.15, A = 50, V = 111.82$.

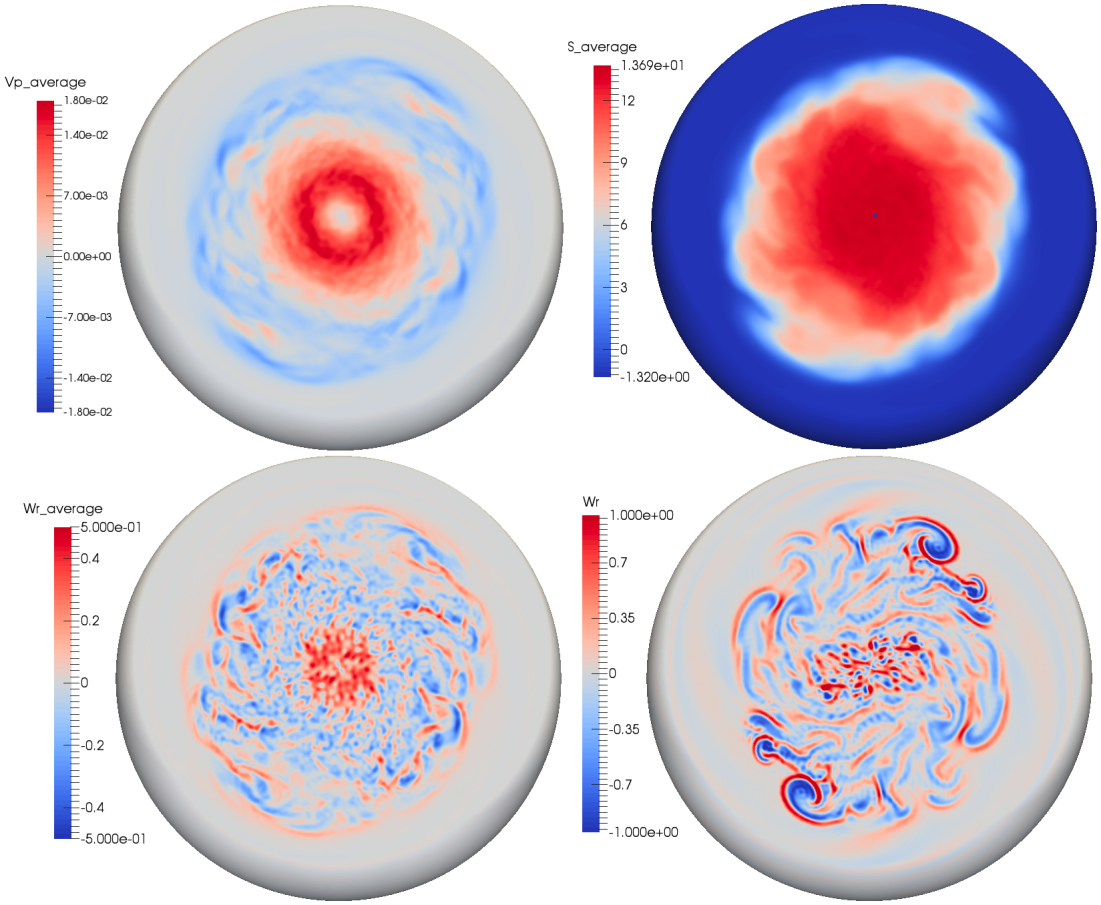

Figure 3.11: Time-averaged azimuthal velocity (top left), time-averaged entropy (top right), time-averaged radial vorticity (bottom left), and radial vorticity snapshot (bottom right) for case 3.3.15 with $\sigma = 0.15, A = 200, V = 236.24$.

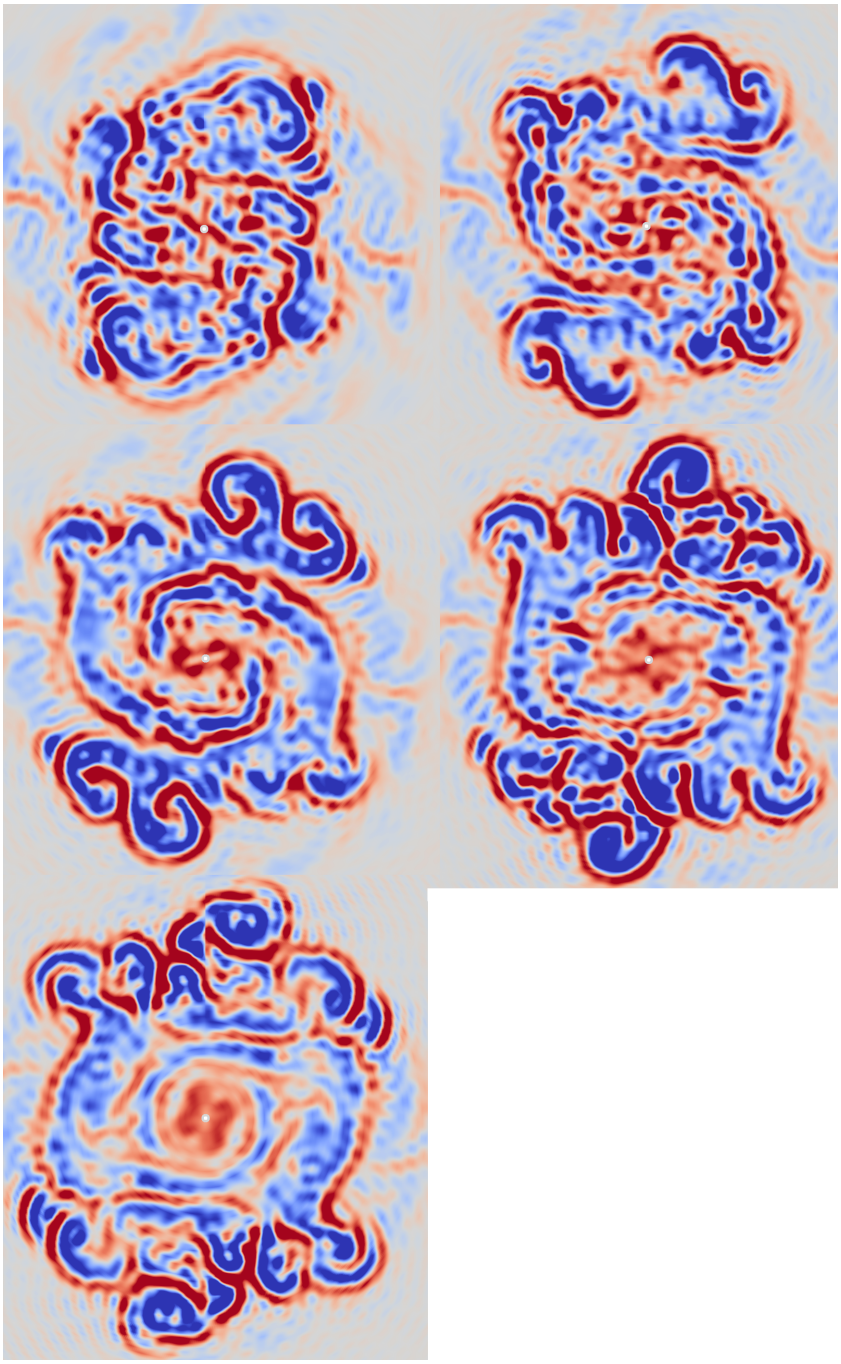

Figure 3.12: Time evolution of radial vorticity for case 3.3.10. Vorticity is scaled to the planetary vorticity. Antiyclonic vorticies shielded by cyclonic filiments migrate to lower latitude.

Chapter 4

Planetary Applications

In this chapter we examine models that are in a parameter space closer to planetary. Rather than using an exponential density profile and an ideal gas for the equation of state we use an polynomial expansion of an empirical model of the interior of Saturn. The empirical model is constrained to match the first three gravitational coefficients and the assumed rate of rotation (Helled et al., 2009). For our model the interior is cut so that 99% of the atmosphere from the molecular envelope up to the 1 bar level is covered. The Ekman number for these models is $E = 10^{-5}$; lower than the previous models. This allows for longer lived vortices zonal flow at higher latitudes. The Rayleigh number is set so that the system is strongly convecting with $Ra^* = 0.45$ and the Prandtl number is set to $Pr = 1$. The radius ratio is set to 0.82, similar to the expected ratio for Saturn. This is based on the location of Saturn's first retrograde jet at a latitude of $\sim 35^\circ$ which corresponds to a tangent cylinder at a radius of $r = \cos(35^\circ) = 0.82$.This requires a high resolution with $N_r = 193$ points in the radial direction, $N_\theta = 576$ points in latitude, and $N_\phi = 1152$ points azimuthally. We are interested in the dynamics at the pole and therefore do not employ spherical harmonic symmetry. For models such as this with a low Ekman number

hyperdiffusion is often required to ensure convergence of the solution. The hyperdiffusion operator is shown in equation (1.51). For this particular case we use an hyperdiffusivity amplitude $\alpha = 60$, hyperdiffusivity exponent $\beta = 3$. The maximum degree of spherical harmonic expansion is $l_{max} = 384$. The amplitude of the hyperdiffusion scaled by the Ekman number is shown in figure 4.1 as a function of spherical harmonic degree l. The high order coefficients are effectively damped to a higher Ekman number while the lower order coefficients remain unchanged.

4.1 Polygonal Jets

Under some circumstances a high latitudinal zonal jet may be convectively forced into a polygonal shape. In this particular case our model is kicked by a change in the background conductive state which provides a initial burst in the poloidal energy. However, in the long term the kinetic energy is weaker and the burst decays. This kick is not particularly physical, however we document it because this is a high resolution run that is computationally expensive and yielded interesting results. The hexagon at the north pole of Saturn as observed by the Cassini spacecraft is shown in figure 4.9. The azimuthal velocity for a model forced by an initial kick in energy is shown in figure 4.2. The evolution of the kinetic energy shortly after the kick is shown in figure 4.9. Shortly after the kick at the peak of energy the high latitude prograde jet is organized in the shape of a heptagon. The flow prograde flow near the pole is almost square shaped. As the energy begins to decay the jet weakens and oscillates about the points of the heptagon. The flow returns to a heptagonal shape, however the jet is weaker and disjoint. The second jet at lower latitude remains relatively stable only weakening slightly as the toroidal energy decays. This jet does not organize into a polygonal shape however sometimes it appears to bend at an angle.

In the long term the high latitude jets are not well maintained and merge such that

there are no distinct jets. The zonal flow observed for Saturn by the Cassini spacecraft and the voyager missions is compared to our results in figure 4.8. There are about 17 jets observed for Saturn that alternate between prograde and retrograde. This is much more than the 7 jets observed for this model. Previous anelastic models using constant entropy boundary conditions with a similar radius ratio (0.85) and the same Ekman number (10^{-5}) have managed to achieve up to 11 jets Gastine et al. (2014). The modified Rayleigh number used for their results is $Ra^* = 0.18$ is much smaller than the $Ra^* = 0.45$ we use. It may be the case that strong convection is required to generate high latitude jets. Although the modified Rayleigh number they use is smaller than ours the conductive state (figure 2.1) means it is convecting much more viperously at the surface.

4.2 Relaxation Oscillations

The kinetic energy in the long term after the kick in energy is shown in figure 4.3. There is initially a sharp decay in the poloidal component of the energy. However shortly after the perturbation it begins to rise again and begins to exhibit periodic relaxation oscillations. The toroidal component of the energy decays much slower over the entire duration of the simulation. There are some small periods when the toroidal energy increases in response to the increased convection of the relaxation oscillations.

The radial vorticity and azimuthal velocity at the poles over the course of a relaxation oscillation is shown in figures 4.4-4.6. There is a strong generation of anticyclonic vortices in the northern hemisphere at the peak of convection shown in figure 4.4. The azimuthal velocity does not have clearly defined jets at higher latitudes and the flow is generally prograde over the pole. Compared to the north pole there is little vortex activity at the south pole for this convective burst. The radial vorticity and zonal flow when the poloidal kinetic energy is at a minimum is shown in figure 4.5. The azimuthal flow in the polar

region is smoother compared to the previous figure. There may be a single high latitude prograde jet that is separated from the pole by a local minimum. The radial vorticity and azimuthal velocity at the next peak in poloidal energy is shown for the south pole in figure 4.6. This time most of the convective activity manifests as anticyclonic storms in the southern hemisphere and the northern hemisphere is comparatively quiet. There is a single high latitude prograde jet with weak retrograde flow towards the pole. The azimuthal flow is distinct between the two poles because they are inside the tangent cylinder and are therefore dynamically disconnected.

The Great White Spot (GWS) storms that are observed on Saturn roughly every Saturnian year are similar to these relaxation oscillations. The 2010 storm on Saturn observed by the Cassini spacecraft may be a GWS as shown in figure 4.10. The GWS is a large storm that encircles the planet and disrupts the latitudinal band that it emerges in. At the peak of a relaxation oscillation there is a latitudinal band that is engulfed by many smaller storms. These storms alternate between a northern latitude band and a souther latitudinal band between oscillations. While all of the GWS storms have been observed in the northern hemisphere they tend to alternate between mid-latitude and equatorial regions Sanchez-Lavega (1994).

The connection between the anticyclonic storms in the northern hemisphere to convection in the interior is shown in figure 4.7. Thermal plumes rise from the interior to the surface where it diverges and forms anticyclonic storms in the northern hemisphere. The storms exist for the duration of the plume and viscously decay shortly after they disconnect. Models that have a lower Ekman number may have storms that can persist for much longer.

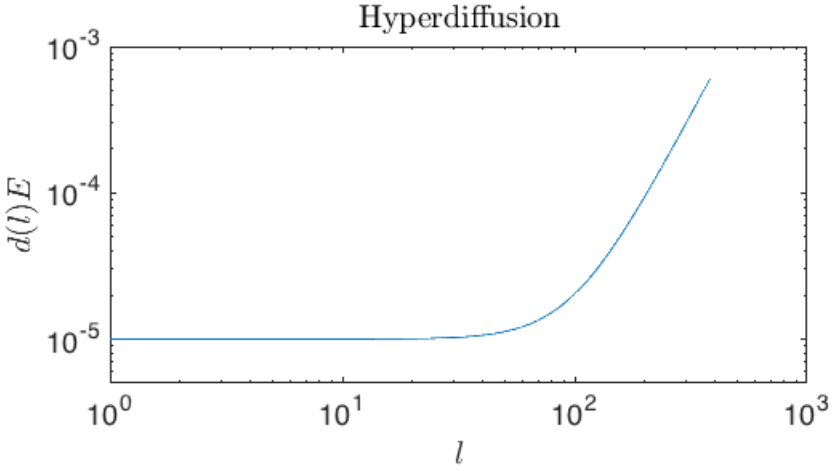

Figure 4.1: Hyperdiffusion amplitude scaled by the Ekman number as a function of spherical harmonic degree l. The hyperdiffusion acts to damp the higher order coefficients which can be interpreted as increasing the Ekman number.

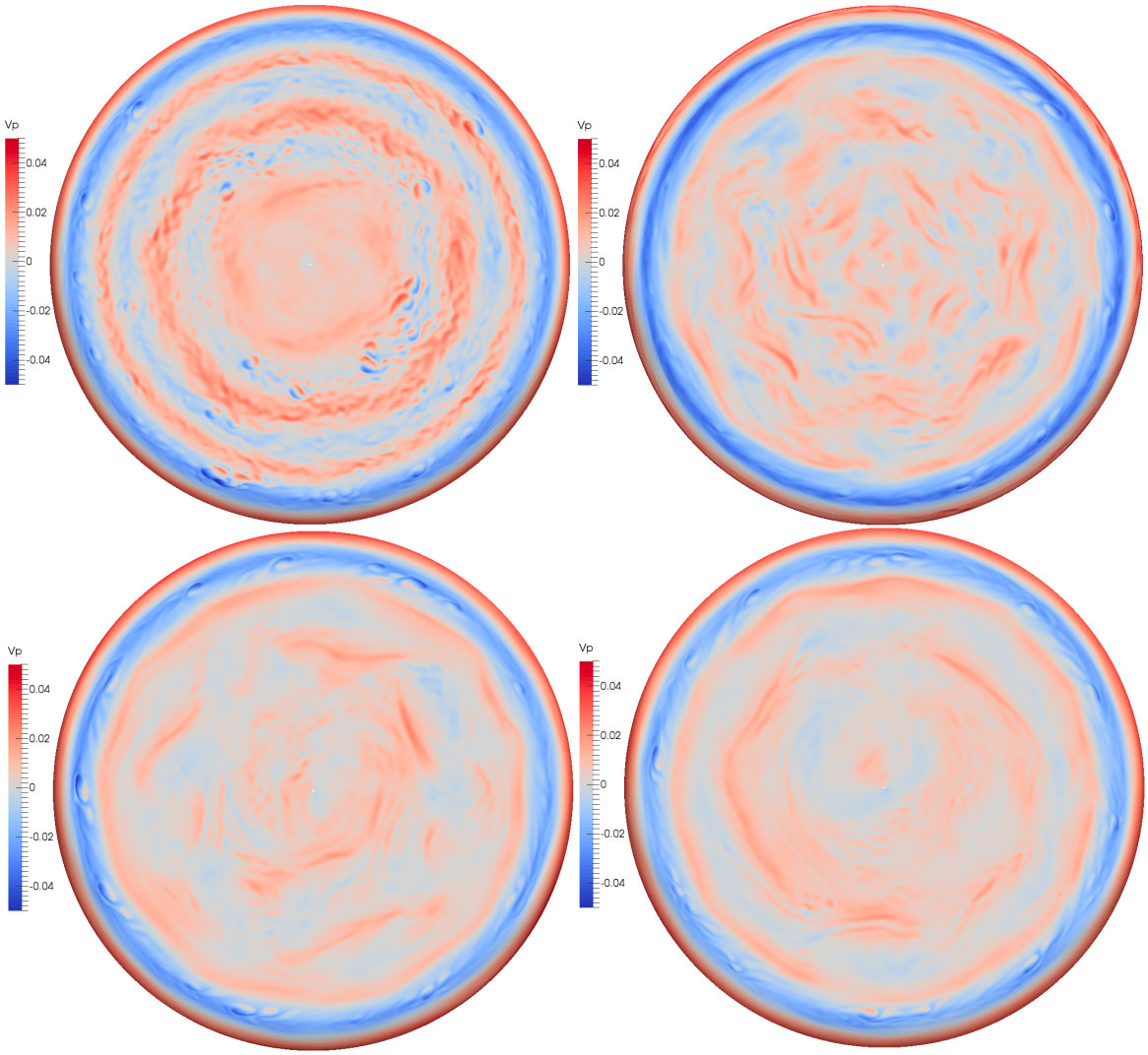

Figure 4.2: Azimuthal velocity that shows high latitude jet numerically forced into a polygonal shape. The heptagon is not stable in time and decays until the jet is lost.

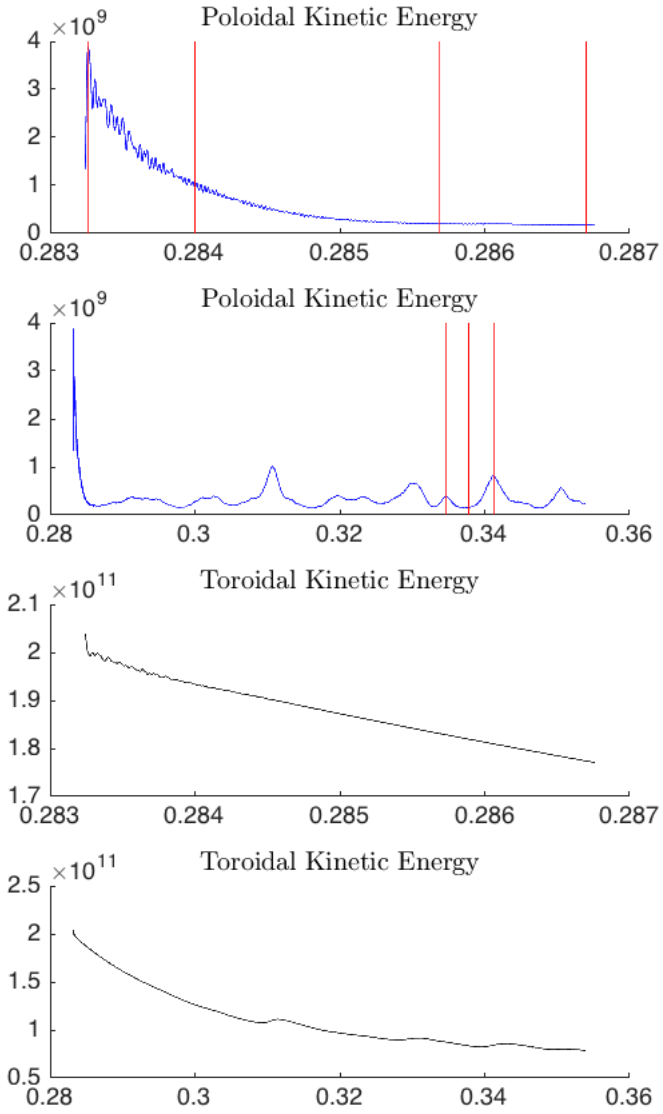

Figure 4.3: Kinetic energy timeseries of Saturn model initially kicked numerically as it decays. The poloidal kinetic energy is shown in blue for the initial kick in energy (top) and for the long term (bottom). The kinetic energy timeseries for the toroidal component is shown in black for the initial kick (top) and for the long term (bottom). Red vertical lines show the position for figures 4.2 and 4.4 - 4.6.

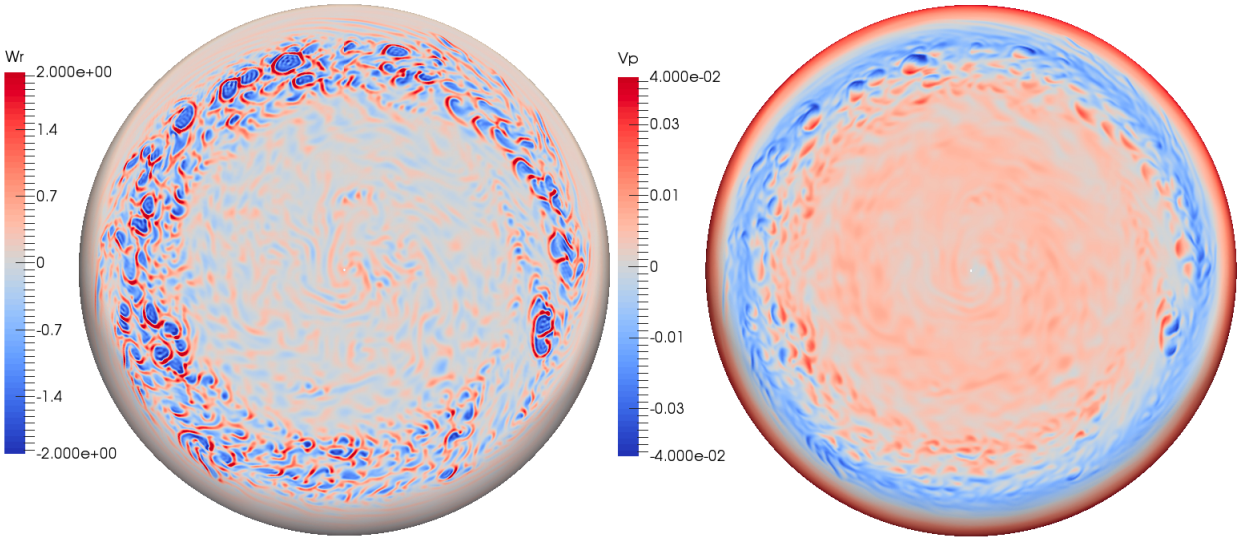

Figure 4.4: Radial vorticity and azimuthal velocity at the north pole at time t=0.3346.

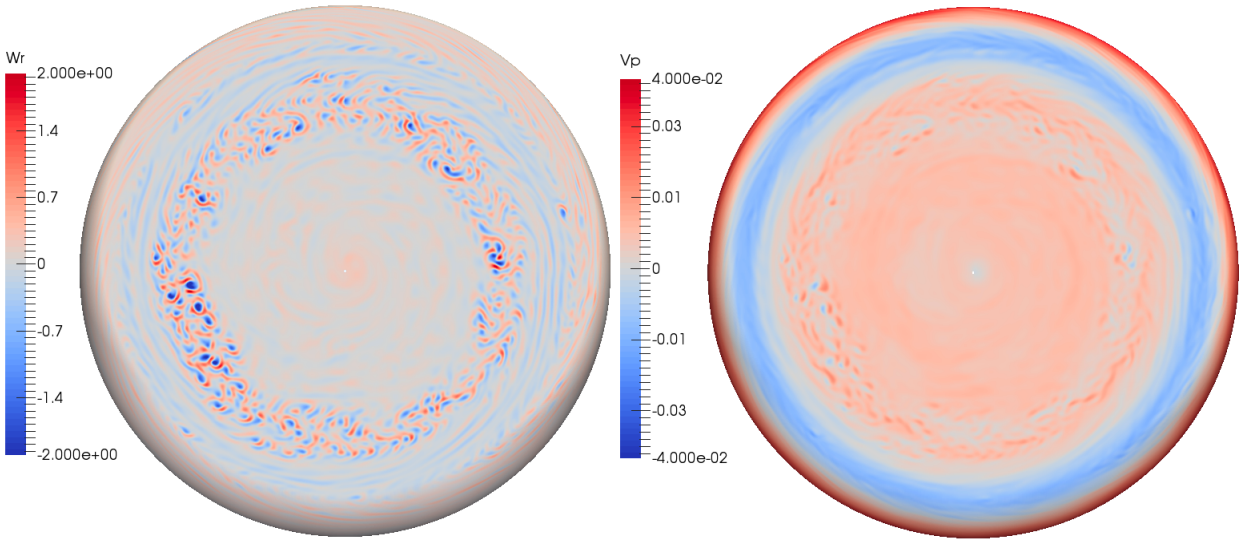

Figure 4.5: Radial vorticity and azimuthal velocity at the north pole at time t=0.3378.

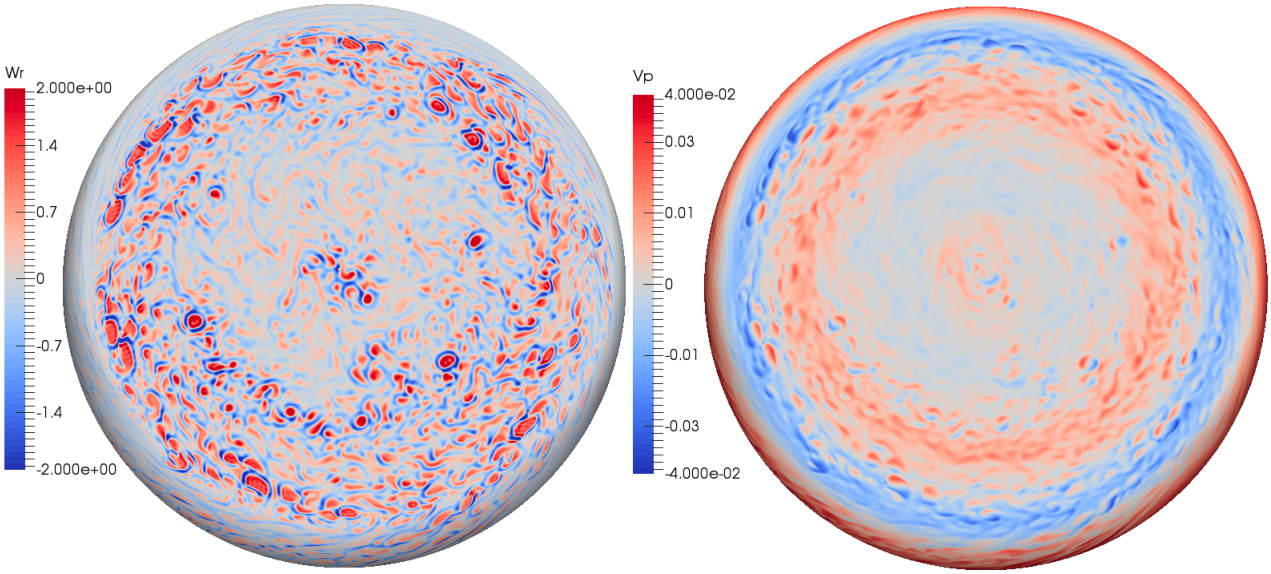

Figure 4.6: Radial vorticity and azimuthal velocity at the south pole at time t=0.3412.

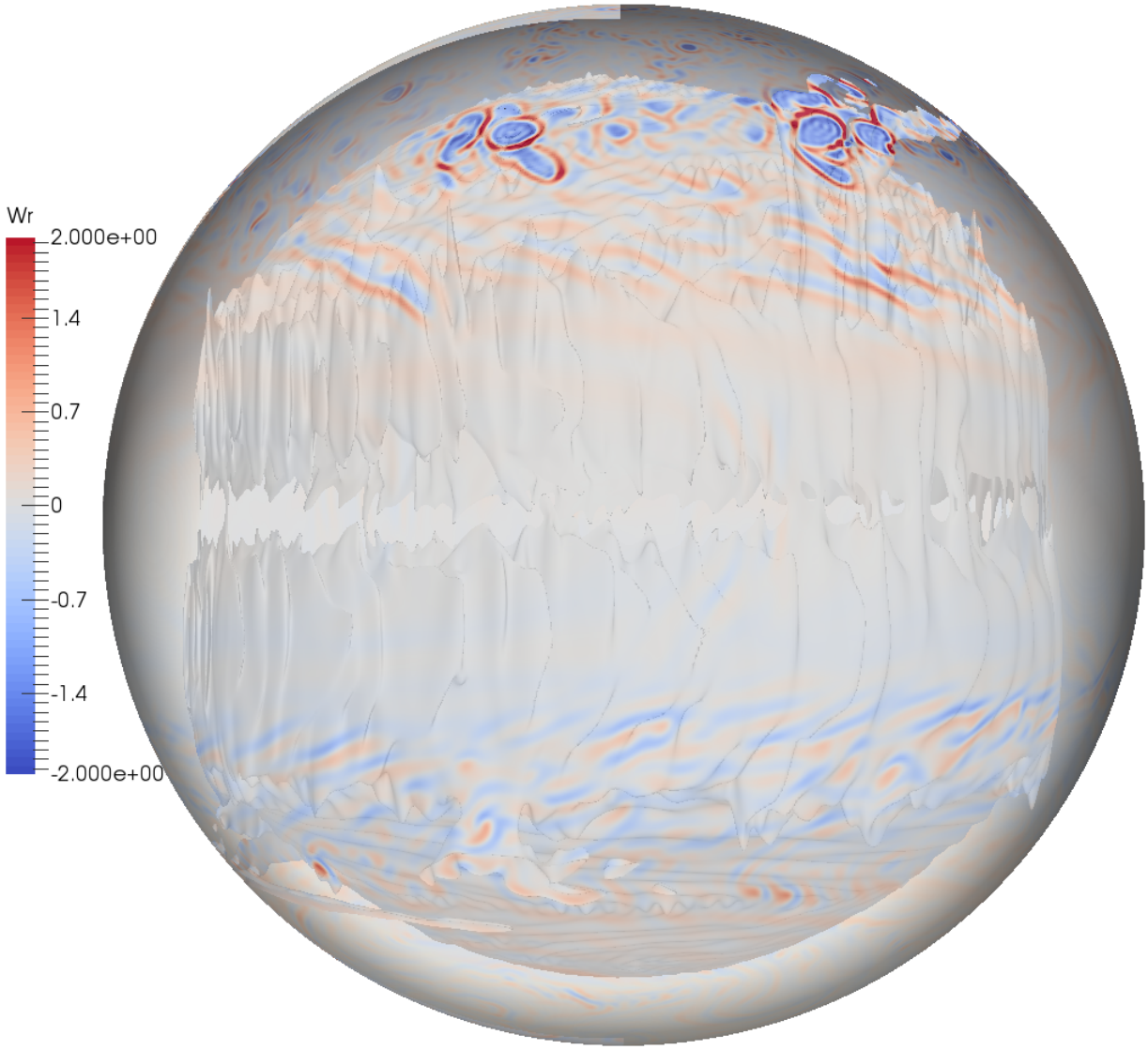

Figure 4.7: Convective cyclonic storms shielded by anticyclonic ring. Entropy isosurface shows the storms connection to the deep interior. The image is taken at a time t=0.3439 roughly halfway between the relaxation oscillation.

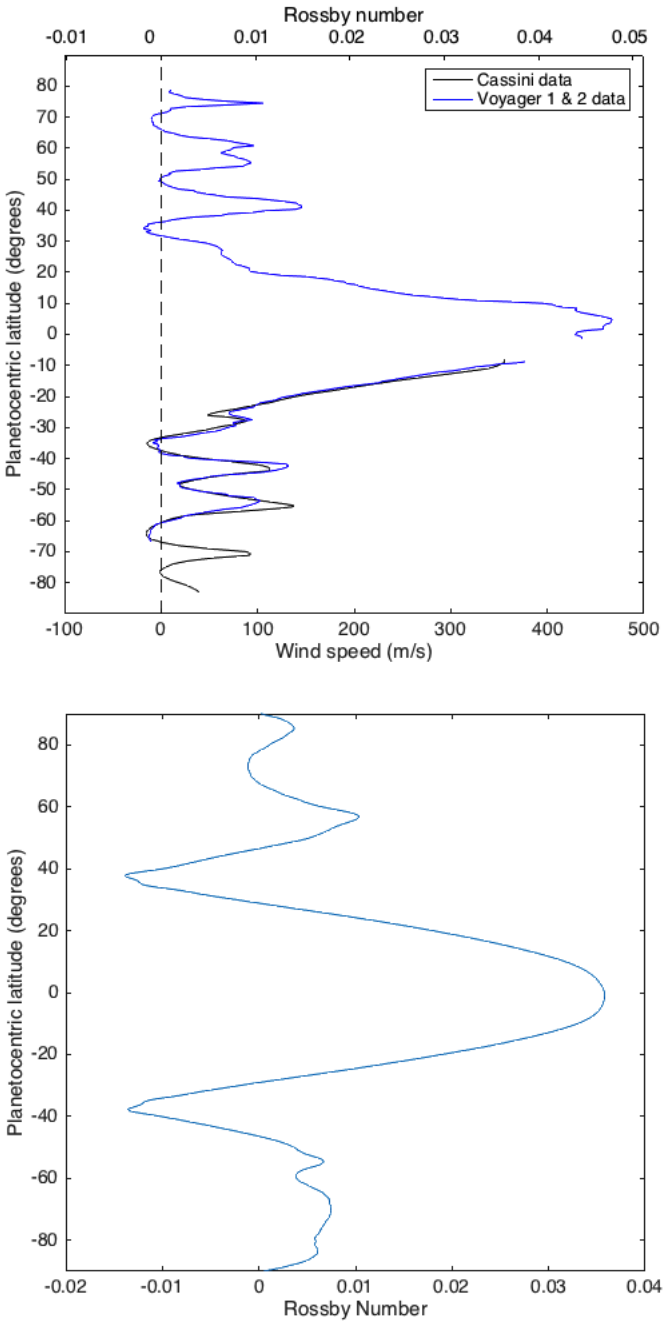

Figure 4.8: Comparison of the zonal flow observed for Saturn by the Cassini and Voyager probes to the flow for our model.

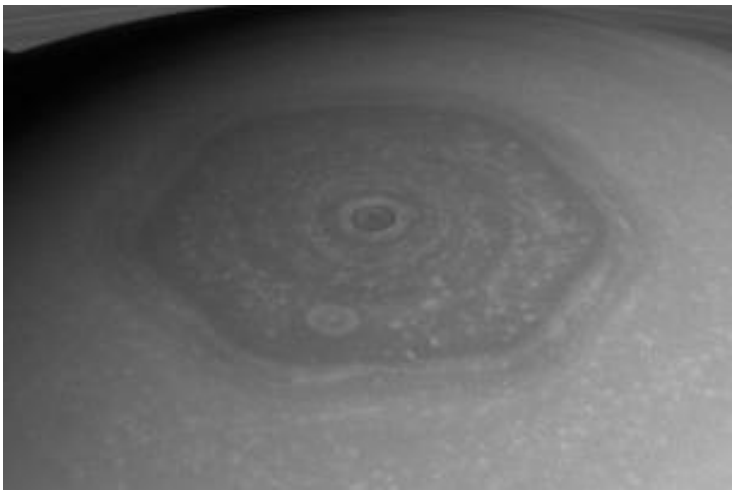

Figure 4.9: Saturn's north polar hexagon as observed by the Cassini spacecraft.

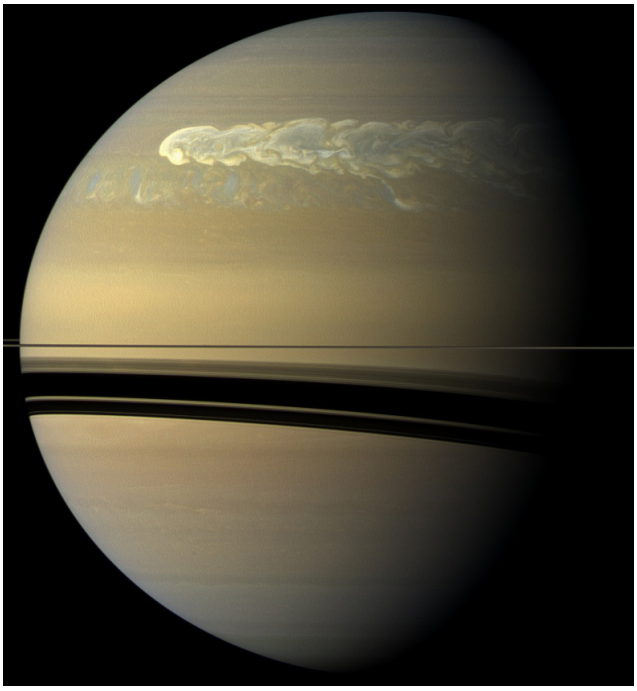

Figure 4.10: Saturn's great storm of 2010 as observed by the Cassini spacecraft. The head of the storm is moving past its tail.

Chapter 5

Conclusion

In this dissertation we have shown the dependance of the entropy boundary condition for simulations of rotating anelastic convection.

Constant entropy gradient boundary conditions with heat sinks allow for a depth dependent Rayleigh number that grades into buoyant stability at the outer boundary. Previous models used constant entropy boundary conditions in which convection is strongest at the surface. The near onset of convection for entropy gradient boundary conditions is similar to previous Boussinesq cases where convection cells form at the inner boundary. Increasing the density stratification increased the number of convection scale but they did not migrate to the outer boundary as in the constant entropy case. The convective regimes observed are similar to previous models however the asymptotic regime is the relaxation oscillation regime rather than a second nonlinear regime. The zonal jets develop is similar for the two boundaries, however the flow is more smooth for the buoyantly neutral case. The entropy gradient boundary conditions allow for the formation of hot regions on the outer boundary that invert the local temperature region and cause regions of dynamic buoyant stability. These regions promote the development of storms or vortices.

Nonhomogeneous boundary conditions can be applied to the lower boundary to examine the potential effects of a thermal plume from the deep interior. A Gaussian shaped perturbation was chosen to model the source because it is a simple shape with an analytic integral. There is a large space of parameters that define the perturbations including offset, amplitude, width, and background Rayleigh number. Regardless of the offset the source will produce a region of stability at the surface axially above the source. The effects of the amplitude and the width of a source were examined, in particular the generation of cyclonic and anticyclonic vortices. It was found that a narrow source with a strong amplitude produces a strong cyclonic storm at the pole similar to observations of Saturn.

Future models of polar nonhomogeneous boundary conditions should consider adjusting the number of grid points in theta so that the spacing is more homogeneous at the poles. This would allow for more efficient use of computational resources. While this may create a similar problem in the equatorial region, if the background Rayleigh number is non-convective it would make no difference. It may also be useful to consider introducing an anomaly into a model with developed zonal jets to see if a jet can be forced locally into a polygonal shape.

Reducing the Ekman number and increasing the radius ratio allows for models that are closer to planetary. However these models are difficult to resolve and require hyperdiffusivity that acts as a low pass filter in the spherical harmonic spectra. High latitude jets can be forced into polygonal shapes under certain circumstances. It is difficult to maintain high latitude jets when using the constant entropy gradient boundary conditions compared to previous models with constant entropy boundary conditions. In the relaxation oscillation convective regime the flow undergoes cycles of strong vorticity that can engulf an entire band latitudinally. This may be similar to the Great White Spot storms that are observed on Saturn with a period of one Saturnian year.

Future models may be able to maintain the polygonal forced jet with a more physical forcing by increasing the strength of convection. This would involve increasing Ra^* so that the system is forced strongly. However current models are already convecting much stronger than planetary and this would move further away. The other alternative to increase the strength of convection while maintaining a smaller Ra^* would be to lower the Ekman number. This is computationally difficult however future massively parallel simulations may allow for a high enough resolution.

Bibliography

Aguiar, A. C. B., Read, P. L., Wordsworth, R. D., Salter, T., and Yamazaki, Y. H. (2010). A laboratory model of saturn's north polar hexagon. *Icarus*, 206(2):755–763.

Allison, M., Godfrey, D., and Beebe, R. (1990). A wave dynamical interpretation of saturn's polar hexagon. *Science*, 247(4946):1061–1063.

Atkinson, D. H., Pollack, J. B., and Seiff, A. (1998). The galileo probe doppler wind experiment: Measurement of the deep zonal winds on jupiter. *Journal of Geophysical Research: Planets*, 103(E10):22911–22928.

Aurnou, J. M. and Heimpel, M. H. (2004). Zonal jets in rotating convection with mixed mechanical boundary conditions. *Icarus*, 169(2):492–498.

Aurnou, J. M. and Olson, P. L. (2001). Strong zonal winds from thermal convection in a rotating spherical shell. *Geophys. Res. Lett*, 28(13):2557–2559.

Baines, K. H., Momary, T. W., Fletcher, L. N., Showman, A. P., Roos-Serote, M., Brown, R. H., Buratti, B. J., Clark, R. N., and Nicholson, P. D. (2009). Saturn's north polar cyclone and hexagon at depth revealed by cassini/vims. *Planetary and Space Science*, 57(14):1671–1681.

Breuer, M., Manglik, A., Wicht, J., Trümper, T., Harder, H., and Hansen, U. (2010). Thermochemically driven convection in a rotating spherical shell. *Geophysical Journal International*, 183(1):150–162.

Busse, F. (1976). A simple model of convection in the jovian atmosphere. *Icarus*, 29(2):255–260.

Busse, F. H. (1970). Thermal instabilities in rapidly rotating systems. *Journal of Fluid Mechanics*, 44(03):441–460.

Christensen, U., Aubert, J., Cardin, P., Dormy, E., Gibbons, S., Glatzmaier, G., Grote, E., Honkura, Y., Jones, C., Kono, M., Matsushima, M., Sakuraba, A., Takahashi, F., Tilgner, A., Wicht, J., and Zhang, K. (2001). A numerical dynamo benchmark. *Physics*

of the Earth and Planetary Interiors, 128(14):25 – 34. Dynamics and Magnetic Fields of the Earth's and Planetary Interiors.

Christensen, U. and Wicht, J. (2007). 8.08 - numerical dynamo simulations. In Schubert, G., editor, *Treatise on Geophysics*, pages 245 – 282. Elsevier, Amsterdam.

Christensen, U. R. (2001). Zonal flow driven by deep convection in the major planets. *Geophysical research letters*, 28(13):2553–2556.

Del Genio, A. D., Achterberg, R. K., Baines, K. H., Flasar, F. M., Read, P. L., Sánchez-Lavega, A., and Showman, A. P. (2009). Saturn atmospheric structure and dynamics. In *Saturn from Cassini-Huygens*, pages 113–159. Springer.

Desch, M. and Kaiser, M. (1981). Voyager measurement of the rotation period of saturn's magnetic field. *Geophysical Research Letters*, 8(3):253–256.

Dyudina, U. A., Ingersoll, A. P., Ewald, S. P., Vasavada, A. R., West, R. A., Baines, K. H., Momary, T. W., Del Genio, A. D., Barbara, J. M., Porco, C. C., et al. (2009). Saturn's south polar vortex compared to other large vortices in the solar system. *Icarus*, 202(1):240–248.

Fortney, J. J. and Nettelmann, N. (2010). The interior structure, composition, and evolution of giant planets. *Space Science Reviews*, 152(1-4):423–447.

French, M., Becker, A., Lorenzen, W., Nettelmann, N., Bethkenhagen, M., Wicht, J., and Redmer, R. (2012). Ab initio simulations for material properties along the jupiter adiabat. *The Astrophysical Journal Supplement Series*, 202(1):5.

Galanti, E. and Kaspi, Y. (2015). An adjoint based method for the inversion of the juno and cassini gravity measurements into wind fields. *Jupiter*, 60:90.

Gastine, T., Heimpel, M., and Wicht, J. (2014). Zonal flow scaling in rapidly-rotating compressible convection. *Physics of the Earth and Planetary Interiors*, 232:36–50.

Gastine, T. and Wicht, J. (2012). Effects of compressibility on driving zonal flow in gas giants. *Icarus*, 219(1):428–442.

Gastine, T., Wicht, J., and Aurnou, J. (2013). Zonal flow regimes in rotating anelastic spherical shells: An application to giant planets. *Icarus*, 225(1):156–172.

Glatzmaier, G. A. (1984). Numerical simulations of stellar convective dynamos. i. the model and method. *Journal of Computational Physics*, 55(3):461–484.

Godfrey, D. (1988). A hexagonal feature around saturn's north pole. *Icarus*, 76(2):335–356.

Godfrey, D. and Moore, V. (1986). The saturnian ribbon feature- a baroclinically unstable model. *Icarus*, 68(2):313–343.

Grote, E. and Busse, F. (2001). Dynamics of convection and dynamos in rotating spherical fluid shells. *Fluid Dynamics Research*, 28(5):349–368.

Guillot, T. and Gautier, D. (2015). 10.16 - giant planets. In Schubert, G., editor, *Treatise on Geophysics (Second Edition)*, pages 529 – 557. Elsevier, Oxford, second edition edition.

Guillot, T., Stevenson, D. J., Hubbard, W. B., and Saumon, D. (2004). The interior of jupiter. *Jupiter. The Planet, Satellites and Magnetosphere*, 1:35–57.

Heimpel, M. and Aurnou, J. (2007). Turbulent convection in rapidly rotating spherical shells: A model for equatorial and high latitude jets on jupiter and saturn. *Icarus*, 187(2):540–557.

Heimpel, M., Aurnou, J., and Wicht, J. (2005). Simulation of equatorial and high-latitude jets on jupiter in a deep convection model. *Nature*, 438(7065):193–196.

Heimpel, M. and Aurnou, J. M. (2012). Convective bursts and the coupling of saturn's equatorial storms and interior rotation. *The Astrophysical Journal*, 746(1):51.

Heimpel, M., Gastine, T., and Wicht, J. (2016). Simulation of deep-seated zonal jets and shallow vortices in gas giant atmospheres. *Nature Geoscience*, 9(1):19–23.

Heimpel, M. and Gómez Pérez, N. (2011). On the relationship between zonal jets and dynamo action in giant planets. *Geophysical Research Letters*, 38(14).

Helled, R., Schubert, G., and Anderson, J. D. (2009). Empirical models of pressure and density in saturn's interior: Implications for the helium concentration, its depth dependence, and saturn's precession rate. *Icarus*, 199(2):368–377.

Howard, L. N. and Drazin, P. G. (1964). On instability of parallel flow of inviscid fluid in a rotating system with variable coriolis parameter journal of mathematics and physics. *Journal of Mathematics and Physics*, 43(1):83–99.

Jones, C. (2007). Thermal and compositional convection in the outer core. *Treatise in Geophysics, Core Dynamics*, 8:131–185.

Jones, C., Boronski, P., Brun, A., Glatzmaier, G., Gastine, T., Miesch, M., and Wicht, J. (2011). Anelastic convection-driven dynamo benchmarks. *Icarus*, 216(1):120–135.

Jones, C. A. and Kuzanyan, K. M. (2009). Compressible convection in the deep atmospheres of giant planets. *Icarus*, 204(1):227–238.

Kageyama, A. and Yoshida, M. (2005). Geodynamo and mantle convection simulations on the earth simulator using the yin-yang grid. In *Journal of Physics: Conference Series*, volume 16, page 325. IOP Publishing.

Kliore, A. J., Patel, I. R., Lindal, G. F., Sweetnam, D. N., Hotz, H. B., Waite, J. H., and McDonough, T. R. (1980). Structure of the ionosphere and atmosphere of saturn from pioneer 11 saturn radio occultation. *Journal of Geophysical Research: Space Physics*, 85(A11):5857–5870.

Lantz, S. and Fan, Y. (1999). Anelastic magnetohydrodynamic equations for modeling solar and stellar convection zones. *The Astrophysical Journal Supplement Series*, 121(1):247.

Liu, J., Goldreich, P. M., and Stevenson, D. J. (2008). Constraints on deep-seated zonal winds inside jupiter and saturn. *Icarus*, 196(2):653–664.

Magalhães, J. A., Seiff, A., and Young, R. E. (2002). The stratification of jupiter's troposphere at the galileo probe entry site. *Icarus*, 158(2):410–433.

Nellis, W., Ross, M., and Holmes, N. (1995). Temperature measurements of shock-compressed liquid hydrogen: implications for the interior of jupiter. *Science*, 269(5228):1249.

Nettelmann, N., Holst, B., Kietzmann, A., French, M., Redmer, R., and Blaschke, D. (2008). Ab initio equation of state data for hydrogen, helium, and water and the internal structure of jupiter. *The Astrophysical Journal*, 683(2):1217.

O'Neill, M. E., Emanuel, K. A., and Flierl, G. R. (2015). Polar vortex formation in giant-planet atmospheres due to moist convection. *Nature Geoscience*, 8(7):523–526.

Orton, G. and Yanamandra-Fisher, P. (2005). Saturn's temperature field from high-resolution middle-infrared imaging. *Science*, 307(5710):696–698.

Rhines, P. B. (1975). Waves and turbulence on a beta-plane. *Journal of Fluid Mechanics*, 69(03):417–443.

Rojas, J. F., Sada, P. V., et al. (2000). Saturn's zonal winds at cloud level. *Icarus*, 147(2):405–420.

Sanchez-Lavega, A. (1994). Saturns great white spots. *Chaos: An Interdisciplinary Journal of Nonlinear Science*, 4(2):341–353.

Sanchez-Lavega, A. (2002). Observations of saturn's ribbon wave 14 years after its discovery. *Icarus*, 158(1):272–275.

Sánchez-Lavega, A. and Battaner, E. (1986). Long-term changes in saturn's atmospheric belts and zones. *Astronomy and Astrophysics Supplement Series*, 64:287–301.

Sánchez-Lavega, A., Colas, F., Lecacheux, J., Laques, P., Parker, D., and Miyazaki, I. (1991). The great white spot and disturbances in saturn's equatorial atmosphere during 1990. *Nature*, 353:397–401.

Sayanagi, K. M., Dyudina, U. A., Ewald, S. P., Fischer, G., Ingersoll, A. P., Kurth, W. S., Muro, G. D., Porco, C. C., and West, R. A. (2013). Dynamics of saturn's great storm of 2010–2011 from cassini iss and rpws. *Icarus*, 223(1):460–478.

Schaeffer, N. (2013). Efficient spherical harmonic transforms aimed at pseudospectral numerical simulations. *Geochemistry, Geophysics, Geosystems*, 14(3):751–758.

Scott, R. and Polvani, L. M. (2008). Equatorial superrotation in shallow atmospheres. *Geophysical Research Letters*, 35(24).

Smith, E., Davis, L., Jones, D., Coleman, P., Colburn, D., Dyal, P., Sonett, C., and Frandsen, A. (1974). The planetary magnetic field and magnetosphere of jupiter: Pioneer 10. *Journal of Geophysical Research*, 79(25):3501–3513.

Sommeria, J., Meyers, S., and Swinney, H. L. (1991). Experiments on vortices and rossby waves in eastward and westward jets. *Nonlinear Topics in Ocean Physics*, 109:227–269.

Vasavada, A. R. and Showman, A. P. (2005). Jovian atmospheric dynamics: An update after galileo and cassini. *Reports on Progress in Physics*, 68(8):1935.

Wicht, J. (2002). Inner-core conductivity in numerical dynamo simulations. *Physics of the Earth and Planetary Interiors*, 132(4):281–302.

Williams, G. P. (1978). Planetary circulations: 1. barotropic representation of jovian and terrestrial turbulence. *Journal of the Atmospheric Sciences*, 35(8):1399–1426.